Journal of Neuroinflammation

RESEARCH

Open Access

Target inhibition of SPAK in choroid plexus attenuates T cell infiltration and demyelination in experimental autoimmune encephalomyelitis

Chenxing Qi[1†], Yeping Wang[2†], Xuhang Li[3†], Cheng Zheng[1], Yi Gu[3], Junxiao Hu[3], Yiming Qiu[3], Guomin Xie[1], Shujun Xu[3,4], Yuyin Zheng[2*], Zhongyue Lv[1*] and Wu Zheng[1,3*]

Abstract

Background Disease-modifying therapies (DMTs) that prevent immune cell infiltration into the brain have demonstrated efficacy in multiple sclerosis (MS) treatment. However, their unpredictable adverse effects necessitate the development of safer therapeutic alternatives. The choroid plexus (ChP) functions as a crucial barrier against immune cell invasion, and previous studies have shown that preventing immune cell infiltration across the ChP reduces brain lesion in MS animal models. Understanding ChP barrier regulation is therefore essential for identifying novel therapeutic targets for MS. Here, we explored the role of Ste20-related proline/alanine-rich kinase (SPAK) in experimental autoimmune encephalomyelitis (EAE).

Methods We examined the expression patterns of SPAK signaling in ChP using immunofluorescence in the EAE model. To investigate the roles of SPAK, matrix metalloproteinase (MMP) 2 and MMP9 in EAE pathology, we performed ChP-specific gene manipulation via intracerebroventricular (ICV) injection of recombinant adeno-associated virus 2/5 (rAAV2/5). T cell infiltration into the central nervous system (CNS) was analyzed using CD4 immunostaining and flow cytometry. We employed cell immunofluorescence, transwell assays, and rescue experiments in vitro to study SPAK's effects on ChP epithelial barrier integrity. We also evaluated the protective effects of SPAK-Na-K-2Cl cotransporter-1 (NKCC1) inhibitors (ZT-1a and bumetanide) on immune invasion and demyelination during EAE using pharmacological approaches.

†Chenxing Qi, Yeping Wang and Xuhang Li contributed equally to this work.

*Correspondence:
Yuyin Zheng
zhyuyin@wzhealth.com
Zhongyue Lv
lzy_neuro@163.com
Wu Zheng
zheng123wu@163.com

Full list of author information is available at the end of the article

Results Following EAE induction, we observed progressive increases in both total and phosphorylated SPAK levels in ChP epithelium. Notably, ChP-specific SPAK knockdown significantly reduced T cell invasion and ameliorated EAE pathology, while SPAK overexpression exacerbated these effects. Bulk RNA sequencing and subsequent qPCR validation revealed that SPAK knockdown decreased the expression of MMP2 and MMP9, MMPs that compromise barrier integrity by degrading tight junction proteins. In vitro studies demonstrated that SPAK overexpression impaired ChP barrier function through the activator protein-1 (AP-1)-MMP2/9-zonula occludens-1 (ZO-1) axis. Furthermore, ChP-specific knockdown of either MMP2 or MMP9 protected against EAE pathology. Additionally, we identified SPAK-NKCC1 antagonists (bumetanide and ZT-1a) as promising therapeutic candidates for MS/EAE treatment.

Conclusions Our findings demonstrate that targeting ChP-SPAK signaling represents a novel therapeutic strategy for MS treatment.

Keywords Choroid plexus, SPAK, Tight junctions, Multiple sclerosis, Experimental autoimmune encephalomyelitis

Introduction

Multiple sclerosis (MS) is a chronic autoimmune disease characterized by demyelination of nerves within the central nervous system (CNS) [1, 2]. This demyelinating process manifests in diverse clinical symptoms, including visual impairments, neuropathic pain, muscular weakness, cognitive dysfunction, and potential long-term disability [3]. While the complete pathogenic mechanisms remain to be fully elucidated, the widespread success of disease-modifying therapies (DMTs) has established immune cell-mediated damage as a central component of MS pathology.

The evolution of MS therapeutics, from first-generation DMTs such as interferon beta to highly efficacious agents including natalizumab, ofatumumab, and alemtuzumab, has validated the strategy of limiting CNS immune cell infiltration as a primary therapeutic approach [4]. However, current DMTs are associated with significant adverse effects, including progressive multifocal leukoencephalopathy, systemic reactions (fever, chills), and gastrointestinal disturbances (nausea), highlighting the urgent need for safer therapeutic alternatives [5, 6]. Recent evidence has challenged the traditional conceptualization of MS as a purely relapsing-remitting disease with complete intermediate recovery, emphasizing the impact of early disease events on long-term patient outcomes [7]. This paradigm shift underscores the critical importance of early therapeutic intervention in MS management.

The choroid plexus (ChP) is a critical structure for maintaining immune privilege in the CNS [8]. Its epithelial tight junctions (TJs) form the blood-cerebrospinal fluid barrier (BCSFB), which limits the entry of biomacromolecules and immune cells into the cerebrospinal fluid (CSF) [8]. Recent findings demonstrate that the ChP serves as an entry point for "first-wave" T cell infiltration, establishing its pivotal role in the pathogenesis of experimental autoimmune encephalomyelitis (EAE) [9]. Using Cre/LoxP genetic systems and recombinant adeno-associated virus 2/5 (rAAV2/5)-mediated gene delivery, we show that selective modulation of immune cell trafficking across the ChP delays disease onset and mitigates EAE pathology [10, 11]. This precise approach underscores the ChP's importance in MS/EAE pathogenesis and highlights the need to dissect the molecular mechanisms regulating immune cell trafficking through this barrier.

Ste20-related proline/alanine-rich kinase (SPAK, also known as STK39 or serine/threonine kinase 39) is a key regulator of iron transport and has been implicated in CSF production by the ChP [12, 13]. Emerging evidence suggests that SPAK upregulation in the ChP contributes to ischemic stroke pathology, with pharmacological inhibition of SPAK reducing ischemic damage [14]. Additionally, SPAK-Na-K-2Cl cotransporter-1 (NKCC1) antagonists have shown therapeutic potential in vascular dementia and spinal cord injury [15, 16]. SPAK has also been linked to other CNS disorders, including schizophrenia and epilepsy [17, 18]. Notably, clinical imaging studies reveal increased ChP volume in MS patients compared to healthy controls [19–21]. Given SPAK's established involvement in cell volume regulation [22], we hypothesize that ChP SPAK signaling plays a key role in MS pathology.

In this study, we investigate the role of ChP SPAK signaling in EAE, a widely used model of MS. Through ChP-specific SPAK knockdown (SPAK-Kd) and overexpression (SPAK-OE) experiments, we demonstrate that SPAK signaling in the ChP plays a critical role in EAE pathology by regulating immune cell infiltration into the CNS. Our findings reveal that SPAK modulates ChP barrier integrity through the activator protein-1 (AP-1)-matrix metalloproteinase (MMP)2/9-TJ axis. Furthermore, we identify SPAK-NKCC1 inhibitors, ZT-1a and bumetanide, as promising therapeutic candidates for MS.

Materials and methods

Animals

Female C57BL/6 mice (8 weeks old, 22-25 g) were purchased from Charles River Laboratories (Beijing, China). The mice were housed in a pathogen-free facility under

controlled temperature and humidity conditions, with a standard 12-h light/dark cycle and ad libitum access to food and water. All experimental procedures were conducted in accordance with ethical guidelines and approved by Animal Care and Use Committee of Zhejiang Huitong Test & Evaluation Technology Group.

Experimental design

The mice were randomly assigned to experimental groups based on their age and weight. No statistical differences in age or weight were observed among the groups. All researchers conducting the experiments were blinded to group assignments to ensure unbiased results.

Experiment 1: A total of 54 mice were used to investigate temporal changes following EAE induction. Mice were sacrificed at six time points (days 0, 4, 8, 12, 16, and 20), with 9 mice at each time point. Of these, 5 mice were used for immunofluorescence staining, and 4 were used for Western blot analysis.

Experiment 2: A total of 44 mice were used to study the effects of SPAK-Kd. The mice were randomly divided into two groups: scramble control ($n = 22$) and SPAK-Kd ($n = 22$). Following virus delivery via intracerebroventricular (ICV) injection and EAE induction, mice were sacrificed for analysis at three time points: 10 mice from each group on day 14, 5 mice on day 21, and the remaining 7 mice on day 25.

Experiment 3: A total of 34 mice were used to examine the effects of SPAK-OE. The mice were randomly divided into two groups: control ($n = 17$) and SPAK-OE ($n = 17$). After ICV virus injection and EAE induction, mice were sacrificed for analysis at three time points: 5 mice from each group on day 14, 5 mice on day 21, and the remaining 7 mice on day 25.

Experiment 4: A total of 20 mice were randomly assigned to four groups: untreated ($n = 5$), control ($n = 5$), SPAK-Kd ($n = 5$), and SPAK-OE ($n = 5$). Mice in the control, SPAK-Kd, and SPAK-OE groups underwent EAE induction two weeks after ICV virus injection, while mice in the untreated group did not receive EAE induction. All mice were sacrificed for sampling on day 14 post-EAE induction (or at the equivalent time point for the untreated group).

Experiment 5: A total of 108 mice were randomly divided into four groups: untreated ($n = 27$), scramble control ($n = 27$), MMP2 knockdown (MMP2-Kd, $n = 27$), and MMP9 knockdown (MMP9-Kd, $n = 27$). Mice in the scramble, MMP2-Kd, and MMP9-Kd groups received ICV virus injections two weeks prior to EAE induction, while the untreated group did not undergo EAE induction. Fifteen mice from each group were sacrificed on day 14 post-EAE induction, 5 mice on day 21, and the remaining 7 mice on day 25.

Experiment 6: A total of 44 mice were randomly divided into two groups: vehicle ($n = 22$) and ZT-1a ($n = 22$). Following EAE induction, 10 mice from each group were sacrificed on day 14, 5 mice on day 21, and the remaining 7 mice on day 25 post-EAE induction.

Experiment 7: This experiment was conducted in three parts, involving a total of 82 mice. In the first part, 14 mice were randomly assigned to vehicle ($n = 7$) and bumetanide (intraperitoneal injection, daily; $n = 7$) groups after EAE induction. Mice were sacrificed on day 25 post-EAE induction. In the second part, 34 mice were randomly divided into vehicle ($n = 17$) and bumetanide (ICV injection, daily; $n = 17$) groups. Five mice from each group were sacrificed on day 14, 5 on day 21, and the remaining 7 on day 25 post-EAE induction. In the third part, 34 mice were randomly assigned to vehicle ($n = 17$) and bumetanide (ICV injection, administered daily from days 8-14 post-EAE induction, $n = 17$) groups. Five mice from each group were sacrificed on day 14, 5 on day 21, and the remaining 7 on day 25 post-EAE induction.

EAE induction and clinical assessment

EAE was induced following previously established protocols [23]. Briefly, anesthetized mice received subcutaneous injections of an emulsion containing myelin oligodendrocyte glycoprotein (MOG_{35-55}) peptide (1 mg/mL in PBS; Anaspec, California, USA) mixed at a 1:1 ratio with complete Freund's adjuvant (CFA; Sigma, Missouri, USA). 200 ng pertussis toxin (500 ng/mL; Absin, Shanghai, China) was administered intraperitoneally at 0 and 48 h post-immunization to enhance disease induction.

Disease severity was assessed daily using a composite scoring system ranging from 0 to 15, based on observed neurological deficits in the tails and limb [23]. Tail assessment: A score of 0 indicates no signs, 1 indicates partial paralysis, and 2 indicates complete paralysis. Limb assessment: A score of 0 indicates no signs, 1 indicates reduced mobility or irregular locomotion, 2 indicates partial paralysis, and 3 indicates complete paralysis. The total EAE score was calculated by summing the tail score and the scores for all four limbs. For example, an animal exhibiting complete paralysis in all four limbs would receive a score of 14. A score of 15 was assigned in cases of mortality.

Target gene manipulation in ChP

To achieve overexpression of SPAK in vivo, the full cDNA of SPAK (*stk39*, mouse) was cloned and inserted into the pAV-CMV-C-3Flag vector (note: SPAK was not fused with a Flag tag). The pAV-CMV-P2A-GFP vector was used as the control for overexpression experiments. For gene knockdown in ChP, designed shRNA or scramble sequences were inserted into the pAV-U6-shRNA-CMV-GFP vector. The shRNA sequences used were as follows:

5'-GTCGAGCGGTCACCTTCATAA-3' (*stk39*), 5'-GACAAGTTCTGGAGATAC-3' (*mmp2*), 5'-CAGTACCAAGACAAAGCCTAT-3' (*mmp9*) and 5'-GCCTAAGGTTAAGTCGCCCTCG-3' (scramble). ChP-specific gene manipulation was performed following previously described methods [11].

Briefly, viral vectors were administered via stereotactic injection into the left lateral ventricle using the following coordinates from the bregma: anterior-posterior + 0.98 mm, medial-lateral − 1.3 mm, and dorsal ventral 2.6 mm. The following rAAV2/5 constructs were obtained from Vigenebio (Shandong, China) in the experiments: rAAV2/5-CMV-SPAK (3.11×10^{12} vg/mL), rAAV2/5-CMV-EGFP (3.42×10^{12} vg/mL), rAAV2/5-U6-shRNA-SPAK-CMV-EGFP (2.79×10^{12} vg/mL), rAAV2/5-U6-shRNA-MMP2-CMV-EGFP (2.93×10^{12} vg/mL), rAAV2/5-U6-shRNA-MMP9-CMV-EGFP (3.06×10^{12} vg/mL), or rAAV2/5-U6-scramble-CMV-EGFP (3.14×10^{12} vg/mL).

Each mouse received a total of 2 μL of viral suspension, injected at a rate of 500 nL/min. To prevent backflow of the injected solution, the injection needle was kept in place for 5 min following delivery. After surgery, mice were placed on a heating pad for one hour to facilitate post-operative recovery and minimize mortality.

Immunofluorescence staining

Mice were deeply anesthetized with pentobarbital and transcardially perfused with sterile PBS, followed by 4% paraformaldehyde (PFA). Harvested brain and spinal cords tissues were post-fixed in PFA and cryoprotected in 30% sucrose for 3 days. Tissues were then embedded in optimal cutting temperature compound and sectioned at 20 μm thickness for brain samples and 40 μm thickness for spinal cord samples.

Tissue sections were washed in PBS and blocked for 2 h at room temperature in a blocking buffer containing 5% donkey serum, 1% BSA, and Triton X-100 (0.1%). Primary antibodies were applied overnight at 4 ℃ and included: rabbit anti-SPAK (1:200, 2281, Cell Signaling Technology, Massachusetts, USA), rabbit anti-phosphorylated SPAK (p-SPAK; 1:200, 07-2273, Millipore, Massachusetts, USA), rabbit anti-phosphorylated NKCC1 (p-NKCC1; 1:200, ABS1004, Millipore, Massachusetts, USA), rat anti-CD4 (1:250, 14-0041-82, Invitrogen, California, USA), rabbit anti-Iba1 (1:400, 019-19741, Wako, Tokyo, Japan), rat anti-CD68 (1:400, MCA1957, Bio-Rad, California, USA), rabbit anti-myelin basic protein (MBP; 1:200, 78896, Cell Signaling Technology, Massachusetts, USA), mouse anti-NF-H (1:200, 2836, Cell Signaling Technology, Massachusetts, USA), mouse anti-MMP2 (1:200, 436000, Invitrogen, California, USA), mouse anti-MMP9 (1:200, MA5-15886, Invitrogen, California, USA), or rabbit anti-zonula occludens-1 (ZO-1; 1:200, 21773-1-AP, Proteintech, Illinois, USA).

After primary antibody incubation, tissue sections were washed with PBS and incubated with appropriate secondary antibodies for 2 h at room temperature. Sections were counterstained with 4',6-diamidino-2-phenylindole (DAPI; Beyotime, Shanghai, China). Three-dimensional microglial morphology was reconstructed using IMARIS 9.0 software.

For CD4 staining, isolated ChP tissues were fixed with 4% PFA for 15 min, transferred to PBS, and processed using the previously described protocol with rat anti-CD4 antibodies (1:250, 14-0041-82, Invitrogen, California, USA). Stained tissues were mounted on glass slides and imaged using a Zeiss LSM900 confocal fluorescence microscope (Baden-Württemberg, Germany).

Cells plated on coverslips were fixed with 4% PFA. After PBS washes, cells were incubated overnight at 4 ℃ with the following primary antibodies: rabbit anti-ZO-1 (1:200, 21773-1-AP, Proteintech, Illinois, USA), rabbit anti-SPAK (1:200, 2281, Cell Signaling Technology, Massachusetts, USA), and rabbit anti-p-SPAK (1:200, 07-2273, Millipore, Massachusetts, USA). Following PBS washes containing Tween 20 detergent (1x PBST), cells were incubated with Alexa Fluor 568-conjugated secondary antibodies (1:500, Abcam, Cambridgeshire, England) for one hour at room temperature. Nuclei were counterstained with DAPI for 10 min before imaging with a fluorescence microscope.

Hematoxylin-eosin (H&E) staining

Mice were deeply anesthetized and transcardially perfused with PBS, followed by 4% PFA. Paraffin-embedded tissue sections were baked at 60 ℃ for 1.5-2 h, then deparaffinized and rehydration through xylene and a graded alcohol series. Antigen retrieval was performed in sodium citrate buffer (pH = 6.0). Sections were sequentially stained with hematoxylin, differentiated in 1% hydrochloric acid-alcohol solution, counterstained with eosin dye solution, and processed through a graded alcohol series and xylene for final clearing.

Quantitative real-time PCR (qPCR)

Total RNA was extracted using Trizol reagent and reverse transcribed into cDNA using the Vazyme cDNA Synthesis Kit (R323-01, Vazyme, Jiangsu, China). PCR amplification was performed using the SYBR Green Kit (RR82LR, Takara, Shiga, Japan) with the following primers: *ppia* (reference gene; forward: 5′-AGCATACAGGTCCTGGCATCTTGT-3′, reverse: 5′-CAAAGACCACATGCTTGCCATCCA-3′), *mmp2* (mouse; forward: 5′-CAAGTTCCCCGGCGATGTC-3′, reverse: 5′-TTCTGGTCAAGGTCACCTGTC-3′), *mmp9* (mouse; forward: 5′-CTGGACAGCCAGACACTAAAG-3′, reverse: 5′-CTCGCG

GCAAGTCTTCAGAG-3′), *mmp2* (rat; forward: 5′-AAG GATGGAGGCACGATTGG-3′, reverse: 5′-GGGAACT TGATGATGGGCGA-3′), *mmp9* (rat; forward: 5′-GCTA TGGTTACACTCGGGCA-3′, reverse: 5′-TGGCCTTTA GTGTCTCGCTG-3′). Target gene expression levels were normalized to the reference gene (*ppia*) using the $2^{-\Delta\Delta Ct}$ method.

Western blotting

ChP tissues or cells were lysed in RIPA buffer supplemented with protease inhibitor (B14001, Bimake, Texas, USA) and phosphatase inhibitor (B15001, Bimake, Texas, USA). Lysates were centrifuged at 10,000 rpm for 10 min, and protein concentrations in the supernatants were determined using a BCA protein assay kit (P0010, Beyotime, Shanghai, China). Samples were denatured in 5X SDS loading buffer (P0015, Beyotime, Shanghai, China) at 90 ℃ for 6 min and separated by SDS-PAGE.

Proteins were transferred to 0.45 μm PVDF membranes (10600023, GE Amersham, Buckinghamshire, UK) at 300 mA for 1 h in ice-cold water. Membranes were blocked with Tris-buffered saline containing 0.1% Tween 20 (TBST) and 1% BSA, then incubated overnight at 4 ℃ with the following primary antibodies: β-Actin (1:2000, 66009-1-Ig, Proteintech, Illinois, USA), SPAK (1:2000, 2281, Cell Signaling Technology, Massachusetts, USA), p-SPAK (1:2000, 07-2273, Millipore, Massachusetts, USA), p-NKCC1 (1:1000, ABS1004, Millipore, Massachusetts, USA), GAPDH (1:2000, GB15004, Servicebio, Hubei, China), c-Fos (1:1000, GB12069, Servicebio, Hubei, China) and c-Jun (1:1000, GB11604, Servicebio, Hubei, China).

After primary antibody incubation, membranes were probed with HRP-conjugated secondary antibodies (1:2000, Cell Signaling Technology, Massachusetts, USA) for 90 min at room temperature. Protein bands were visualized using a Bio-Rad ChemiDoc XRS + molecular imager.

Whole-genome RNA sequencing (RNA-seq)

RNA sequencing libraries were prepared following the manufacturer's protocols (Illumina, USA) and sequenced at ApexBio Technology LLC (Shanghai, China). Sequencing reads were aligned to the mouse reference genome (mm10) using STAR v2.5, and transcript quantification was performed using Homer software (Analyze Repeats). Differential expression analysis was carried out using DEseq2 with five biological replicates per condition. Genes with a $\log_2|\text{fold-change}| > 1.2$ and $P < 0.05$ were considered significantly differentially expressed. Functional annotation of these genes was performed using ClusterProfiler for Gene Ontology (GO) and Kyoto Encyclopedia of Genes and Genomes (KEGG) pathway enrichment analyses.

SPAK overexpression in ChP cell line Z310

The cDNA of rat SPAK gene (*stk39*) was cloned into the FV115 vector (pLent-EF1a-FH-CMV-copGFP-P2A-Puro) and packaged into lentivirus (8×10^8 TU/mL). For viral transduction, Z310 cells (HTX2709, Otwo Biotech, Hubei, China) were seeded at 2×10^5 cells per well in 6-well plates containing DMEM/F12 supplemented with 10% fetal bovine serum. After 24 h, cells were transfected with lentivirus at a multiplicity of infection (MOI) of 50. Stable transformants were selected using puromycin (3 μg/mL). These SPAK-overexpressing cells were used for subsequent experiments.

T cell migration assay

Z310 cells (untreated, SPAK-overexpressing, or empty vector controls) were seeded into the upper chamber of transwell inserts (5 μm pore size, 6.5 mm diameter). CXCL12 (1 μg/mL) was added to the lower chamber as a chemoattractant. For inhibition studies, SPAK-OE cells were treated with either vehicle or an AP-1 inhibitor (SR110302, 1 μM).

For MMP knockdown experiments, SPAK-OE cells were transfected with siRNAs using the GP-transfect-Mate reagent (GenePharma, Jiangsu, China): siMMP2: 5'-CAUACAGGAUCAUUGGUUATT-3' (sense), 5'-UA ACCAAUGAUCCUGUAUGTT-3' (antisense); siMMP9: 5'-GCACUGGGCUUAGAUCAUUTT-3' (sense), 5'-AA UGAUCUAAGCCCAGUGCTT-3' (antisense).

After 3 days of culture, $CD4^+$ T cells were isolated from C57BL/6 mouse spleens using Anti-Mouse CD4 Magnetic Particles (551539, BD, New Jersey, USA). Purified $CD4^+$ T cells (1×10^5 cells) were added to the upper chamber, with CXCL12 (1 μg/mL) in the lower chamber. After 24 h, migrated T cells in the lower chamber were visualized using crystal violet staining.

Flow cytometry (FCM) analysis

CSF samples (10 μL per mouse) were collected from the medullary cistern of EAE mice 14 days post-immunization and immediately placed on ice. After PBS perfusion, spinal cords were harvested and processed into single-cell suspensions. Red blood cells were lysed using lysis buffer (R7757, Sigma, Missouri, USA) for 5 min. Cell suspensions from both spinal cords and CSF were centrifuged at 1000 rpm for 5 min and resuspended in 100 μL of staining buffer (70-S1001, Multisciences, Zhejiang, China).

Samples were blocked with 20 μL of Clear Back FCR blocking reagent (MTG-001, MBL, Aichi, Japan) for 5 min at room temperature. Cells were then stained for 30 min at 4 ℃ with the following fluorochrome-conjugated monoclonal antibodies: FVS780 (565388, BD Horizon, New Jersey, USA), CD3-FITC (11-0032-82, Invitrogen, California, USA), CD4-APC (2376140,

Invitrogen, California, USA), IFN-γ-BV421 (126529, Biolegend, California, USA), and Th17-PE (129804, Biolegend, California, USA).

After staining, cells were washed and centrifuged at 1000 rpm for 5 min, then resuspended in 200 μL of staining buffer. Data acquisition was performed using an Attune NXT flow cytometer (Invitrogen, California, USA) and analyzed with NovoExpress software (Agilent, California, USA).

Enzyme-linked immunosorbent assay (ELISA)

Cell culture medium was centrifuged at 1500 rpm for 10 min at 4 ℃. Supernatants were collected and analyzed for MMP2 and MMP9 protein levels using commercial ELISA kits (BP-E30505 and BP-E30434, respectively, Boyun, Jiangsu, China).

Drug administration

EAE mice received daily intraperitoneal injections of either vehicle, ZT-1a (5 mg/kg, HY-136532, MCE, New Jersey, USA), or bumetanide (5 mg/kg, B3023, Sigma, Missouri, USA). For ICV bumetanide administration, drug delivery cannulas (Kedou Brain-Computer Technology, Guangdong, China) were implanted in the right lateral ventricle and secured with instant adhesive gel. After a two-week recovery period, mice underwent EAE induction. Bumetanide (0.3 mg/mL, 3 μL) or sterile vehicle was infused into the lateral ventricle using a syringe pump (R462, RWD, Guangdong, China) at a rate of 0.6 μL/min for 5 min, either daily or on days 8-14 post-EAE induction.

Statistical analysis

EAE clinical scores across groups were analyzed using two-way repeated measures (RM) ANOVA. Comparisons between two groups were performed using unpaired t-tests, while multiple group comparisons were analyzed with one-way ANOVA. Immunofluorescence quantification was performed using ImageJ, and FCM data were analyzed using FlowJo™ software. Data are expressed as mean ± SEM, with $P < 0.05$ considered statistically significant. All statistical analyses were conducted using GraphPad Prism 9.0.

Results

SPAK signaling is elevated in ChP epithelium during EAE

We investigated SPAK expression patterns in the brain during EAE progression using a MOG_{35-55}-induced mouse model. Immunofluorescence analysis revealed that SPAK expression in the ChP gradually increased from day 8 (pre-onset phase of EAE) through day 20, compared to baseline levels at day 0 (Fig. 1A-B). Similarly, the level of p-SPAK was elevated during days 8-20 (Fig. 1C-D).

Since activated SPAK is known to p-NKCC1 [24], we also examined p-NKCC1 levels and observed increased phosphorylation during the same period (Fig. 1E-F). Morphological analysis confirmed that SPAK-NKCC1 activation was localized to ChP epithelial cells. Western blot analysis further demonstrated that the protein levels of SPAK, p-SPAK, and p-NKCC1 gradually increased from days 8 to 20, consistent with the immunofluorescence results (Fig. 1G-L). These findings suggest that the elevation of SPAK signaling in ChP tissue may be involved in EAE pathological processes.

Selective SPAK knockdown in the ChP attenuates T cell infiltration and EAE pathology

To investigate the specific role of ChP SPAK signaling in EAE, we performed ChP-targeted SPAK-Kd via ICV injection of rAAV2/5-U6-shRNA-SPAK-EGFP (SPAK-Kd) or rAAV2/5-U6-scramble-EGFP (scramble) (Fig. 2A). Fourteen days post-injection, EGFP expression was exclusively detected in the ChP, with no signal in other brain regions (Fig. 2B). Immunostaining confirmed that the SPAK-Kd virus reduced ChP SPAK protein levels by approximately 60% (Fig. 2C).

Following MOG_{35-55} immunization, SPAK-Kd mice developed significantly milder EAE symptoms compared to controls (Fig. 2D). MBP staining on day 21 post-EAE induction revealed reduced demyelination in SPAK-Kd mice (Fig. 2E-F). In the spinal cords, scramble mice showed numerous CD68 and Iba1 double-positive cells, while SPAK-Kd mice exhibited significantly lower numbers of $CD68^+/Iba1^+$ cells (Fig. 2G-H). Three-dimensional reconstruction of microglia revealed distinct differences between groups: microglia in control group displayed enlarged cell bodies with reduced branching and shorter dendrites, whereas microglia in SPAK-Kd group exhibited small cell bodies with increased branching and longer dendrites (Fig. 2I-L). These findings demonstrate that ChP-specific SPAK-Kd effectively attenuates CNS inflammation and ameliorates EAE pathology.

To assess the effect of SPAK-Kd on T cell infiltration, we analyzed ChP tissues at day 14 post-EAE induction, previously identified as the peak of T cell infiltration in the ChP [13]. SPAK-Kd mice exhibited significantly reduced $CD4^+$ T cell accumulation in the ChP compared to controls (note: For CD4 staining in ChP, we used isolated ChP tissues, not brain slices) (Fig. 2M-N). At day 14 post-EAE induction, H&E staining revealed decreased immune cell infiltration in the spinal cords of SPAK-Kd mice (Fig. 2O-P). Similarly, immunofluorescence analysis demonstrated reduced $CD4^+$ T cell infiltration in the spinal cords of SPAK-Kd mice at this time point (Fig. 2Q-R).

To further explore SPAK's role in $CD4^+$ T cell infiltration into the CNS, we collected CSF samples from scramble and SPAK-Kd mice at day 14 post-EAE induction.

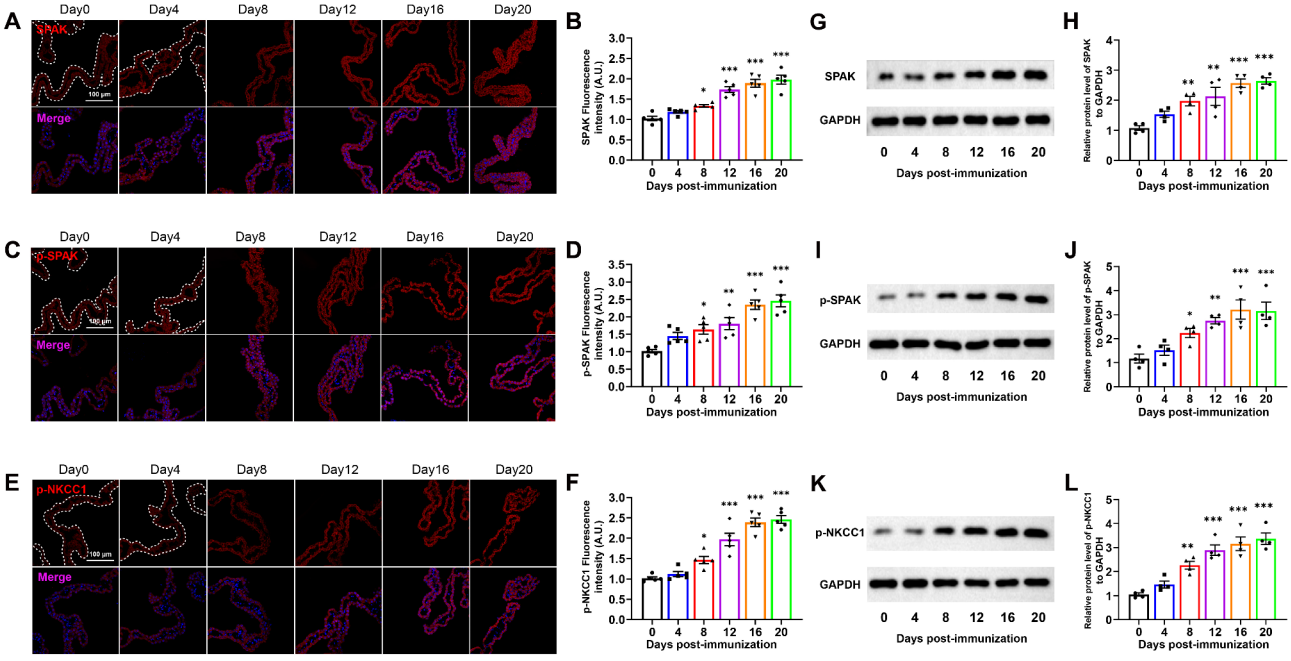

Fig. 1 Temporal Expression Profile of SPAK-NKCC1 Signaling Components in the ChP During EAE Progression. **A.** Representative immunofluorescence images of SPAK expression in the ChP at 0-20 days post-EAE induction. Scale bar: 100 μm. **B.** Quantification of SPAK fluorescence intensity from panel A ($n = 5$/group). **C.** Representative immunofluorescence images of p-SPAK in the ChP at 0-20 days following EAE induction. Scale bar: 100 μm. **D.** Quantification of p-SPAK fluorescence intensity from panel C ($n = 5$/group). **E.** Representative immunofluorescence images of p-NKCC1 in the ChP at 0-20 days post-EAE induction. Scale bar: 100 μm. **F.** Quantification of p-NKCC1 fluorescence intensity from panel E. **G-H.** Representative Western blots and quantification of SPAK protein levels in ChP lysates at 0-20 days post-EAE induction ($n = 4$/group). **I-J.** Representative Western blots and quantification of p-SPAK protein levels in ChP lysates at 0-20 days post-EAE induction ($n = 4$/group). **K-L.** Representative Western blots and quantification of p-NKCC1 protein levels in ChP lysates at 0-20 days following EAE induction ($n = 4$/group). All quantitative data were analyzed using one-way ANOVA with Dunnett's multiple comparisons test. Data are presented as mean ± SEM.* $P < 0.05$, ** $P < 0.01$, *** $P < 0.001$. ChP: choroid plexus

FCM analysis revealed that SPAK-Kd in the ChP significantly reduced CSF $CD4^+$ T cell numbers compared to the scramble group (Fig. 3A-B, Figure S1). Moreover, the numbers of $Th1^+$ and $Th17^+$ T cells, the primary pathogenic T cell subtypes in MS/EAE, were markedly decreased in the CSF of SPAK-Kd mice (Fig. 3C-D). Further analysis of spinal cords tissue at day 14 post-EAE induction confirmed these findings. FCM analysis demonstrated that SPAK-Kd in the ChP significantly reduced CNS infiltration of $CD4^+$, $Th1^+$, and $Th17^+$ T cells (Fig. 3E-H, Figure S2).

SPAK overexpression in the ChP exacerbates T cell infiltration and brain damage

Given the elevated SPAK signaling observed in EAE, we hypothesized that increased ChP SPAK expression would accelerate disease progression. To test this, we induced ChP-specific SPAK-OE via ICV injection of rAAV2/5-CMV-SPAK (SPAK-OE) or rAAV2/5-CMV-EGFP (Control) (Fig. 4A). Fourteen days post-injection, SPAK-OE mice showed significantly higher ChP SPAK protein levels compared to controls, with enhanced SPAK fluorescence exclusively localized in the ChP (Fig. 4B-C). Following MOG_{35-55}/CFA immunization, SPAK-OE mice developed significantly more severe EAE symptoms compared to controls (Fig. 4D). At day 21 post-EAE induction, MBP staining revealed more extensive demyelination in SPAK-OE mice (Fig. 4E-F). Additionally, H&E staining demonstrated markedly increased immune cell infiltration in the spinal cords of SPAK-OE mice (Fig. 4G-H).

Furthermore, SPAK-OE mice exhibited enhanced inflammation, evidenced by an increased number of $CD68^+/Iba1^+$ double-positive cells in the spinal cords (Fig. 4I-J). Analysis of ChP tissue at day 14 post-EAE induction revealed increased $CD4^+$ T cell accumulation in SPAK-OE mice, indicating enhanced T cell infiltration across the ChP barrier (Fig. 4K-L). These findings demonstrate that elevated ChP SPAK signaling exacerbates EAE pathology by promoting T cell infiltration and CNS damage.

SPAK regulates the ChP barrier via AP-1-MMP2/9-TJs axis

To investigate SPAK's potential role in EAE pathogenesis, we performed bulk RNA sequencing on ChP tissue from SPAK-Kd and scramble mice at day 14 post-EAE induction. Analysis identified 1515 differentially expressed genes (DEGs), including 260 upregulated and 1255

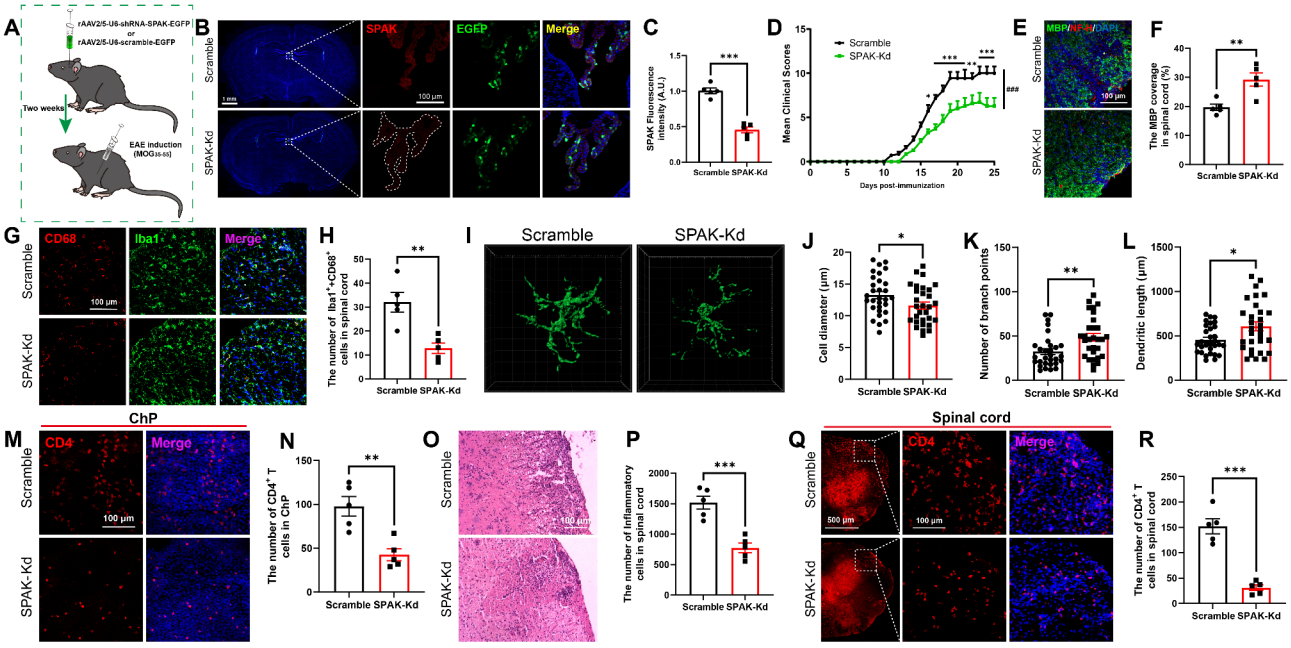

Fig. 2 ChP-Specific SPAK Knockdown Ameliorates EAE Pathology. **A.** Schematic timeline of experimental design for investigating ChP-specific SPAK-Kd effects in the EAE model. **B.** Representative immunofluorescence images showing EGFP expression confined to the ChP 14 days after ICV injection of scramble or SPAK-Kd virus. **C.** Quantification of SPAK fluorescence intensity from panel B ($n = 5$/group). **D.** Clinical disease scores show attenuated EAE severity in ChP SPAK-Kd mice compared to controls ($n = 7$/group). Analysis by two-way RM ANOVA with Sidak's multiple comparisons test. **E.** Representative immunostaining of myelin (MBP) and neuronal (NF-H) markers in spinal cord sections from scramble and SPAK-Kd mice at day 21 following EAE induction. Scale bar: 100 μm. **F.** Quantification of MBP coverage from panel E ($n = 5$/group). **G.** Representative co-immunostaining of microglial markers Iba1 and CD68 in spinal cord sections from scramble and SPAK-Kd mice at day 14 post-EAE induction. Scale bar: 100 μm. **H.** Quantification of Iba1$^+$/CD68$^+$ double-positive microglia from panel G ($n = 5$/group). **I.** Three-dimensional reconstruction of microglial morphology in spinal cords at day 14 post-EAE induction. **J-L.** Morphometric analysis of microglia from panel I: cell diameter (**J**), branch points (**K**), and dendritic length (**L**) ($n = 30$ cells/group). **M.** Representative CD4 immunostaining in ChP tissue at day 14 following EAE induction. Scale bar: 100 μm. **N.** Quantification of CD4$^+$ T cells from panel M ($n = 5$/group). **O.** Representative H&E staining of spinal cord sections from scramble and SPAK-Kd mice at day 14 post-EAE induction. Scale bar: 100 μm. **P.** Quantification of immune cell infiltration from panel O ($n = 5$/group). **Q.** Representative CD4 immunostaining in spinal cords at day 14 following EAE induction. Scale bar: 100 μm. **R.** Quantification of CD4$^+$ T cells from panel Q ($n = 5$/group). Statistical analyses performed using unpaired t-test unless otherwise specified. Data are presented as mean ± SEM. $^{###}P < 0.001$, * $P < 0.05$, ** $P < 0.01$, *** $P < 0.001$. ChP: choroid plexus

downregulated genes. A heatmap of the top 50 DEGs revealed significantly reduced transcript levels of MMP2 and MMP9 in SPAK-Kd samples (Fig. 5A-B). The mRNA level of SPAK (*stk39*) was also significantly reduced in the SPAK-Kd group (Fig. 5A-B). GO annotation highlighted significant enrichment of pathways related to cell junction assembly, which are essential for barrier function (Fig. 5C). Since MMPs compromise barrier integrity by degrading TJs, we hypothesized that SPAK regulates T cell infiltration by modulating MMP2/9-mediated ChP barrier function. The qPCR analysis confirmed reduced MMP2 and MMP9 mRNA expression in SPAK-Kd samples (Fig. 5D-E).

To determine whether these pathway changes were directly due to SPAK-Kd rather than secondary to symptom improvement, we analyzed ChP tissue from mice receiving ICV injection of SPAK-Kd or scramble virus for 14 days without EAE induction. The qPCR confirmed that SPAK-Kd directly reduced MMP2 and MMP9 mRNA levels (Fig. 5F-G). At day 14 post-EAE induction, control EAE mice showed elevated MMP2 and MMP9 protein levels, whereas SPAK-Kd significantly reduced their expression (Fig. 5H-I). Conversely, SPAK-OE further increased MMP2 and MMP9 expression (Fig. 5H-I). To further investigate SPAK's effects on TJs, we analyzed ZO-1 distribution via immunostaining. EAE mice exhibited a marked ZO-1 loss in the ChP (Fig. 5J). Notably, SPAK-Kd partially prevented this ZO-1 loss, whereas SPAK-OE exacerbated it (Fig. 5J).

Under physiological conditions without EAE induction, SPAK-Kd reduced MMP2 and MMP9 protein levels, while enhancing ZO-1 expression in the ChP (Fig. 5N-O). In contrast, SPAK-OE increased MMP2 and MMP9 expression and disrupted ZO-1 distribution in the ChP (Fig. 5N-S).

In vitro, we established a stable SPAK-overexpressing rat ChP epithelial cell line (Z310) Fig. 6A, Figure S3A-D). SPAK-OE led to a significant loss of cellular ZO-1 distribution, indicating compromised barrier integrity between ChP epithelial cells Fig. .6B-C). Treatment of SPAK-OE cells with either siMMP2 or siMMP9 partially restored normal ZO-1 distribution Fig. .6D-G).

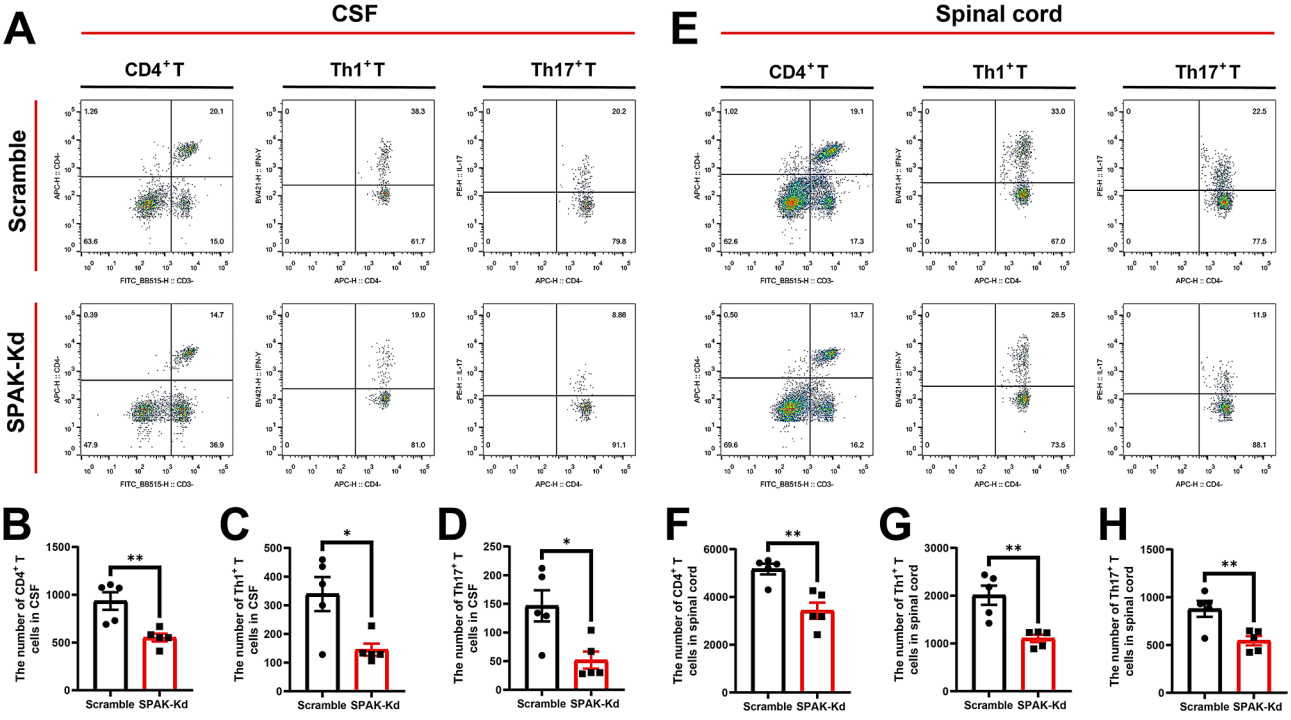

Fig. 3 ChP-Specific SPAK Knockdown Reduces CNS Infiltration of CD4$^+$ T Cell Subsets. **A.** Representative FCM plots showing CD4$^+$, Th1$^+$, and Th17$^+$ T cell populations in CSF at day 14 post-immunization in scramble and ChP-specific SPAK-Kd mice. **B-D.** Quantitative analysis of CSF FCM data showing reduced infiltration of CD4$^+$ (**B**), Th1$^+$ (**C**), and Th17$^+$ (**D**) T cells following ChP-specific SPAK-Kd ($n = 5$/group). **E.** FCM analysis of CD4$^+$, Th1$^+$, and Th17$^+$ T cell populations in spinal cords at day 14 post-immunization in scramble and ChP-specific SPAK-Kd mice. **F-H.** Quantitative analysis of spinal cords FCM data showing reduced infiltration of CD4$^+$ (**F**), Th1$^+$ (**G**), and Th17$^+$ (**H**) T cells at day 14 post-immunization ($n = 5$/group). Statistical analyses performed using unpaired t-test. Data are presented as mean ± SEM. * $P < 0.05$, ** $P < 0.01$. ChP: choroid plexus

Previous research identified AP-1 as a downstream transcript factor of SPAK in T cells [25]. Consistent with these findings, Western blot analysis showed that SPAK-OE increased c-Fos and c-Jun protein levels in the Z310 cell line (Fig. 6H-K). Treatment with the AP-1 inhibitor SR110302 (1 μM) partially restored ZO-1 distribution in SPAK-OE cells (Fig. 6L-M). ELISA analysis further revealed that SPAK-OE increased MMP2 and MMP9 levels in Z310 cells, while AP-1 inhibition prevented this increase (Fig. 6N-Q, Figure S3E-F).

Transwell experiments evaluating ChP barrier function showed that SPAK-OE enhanced CD4$^+$ T cell migration across Z310 cells (Fig. 6R-S). Notably, both MMP2/9 knockdown and AP-1 inhibition reduced T cell migration in the SPAK-OE group (Fig. 6R-S). These findings demonstrate that SPAK signaling regulates ChP barrier integrity and T cell infiltration through the AP-1-MMP2/9-TJs axis.

Selective MMP2/9 knockdown in the ChP attenuates EAE pathology

To further validate the role of the SPAK-AP-1-MMP2/9-TJs axis in EAE pathology, we performed ChP-specific knockdown of MMP2 or MMP9 using ICV injection of rAAV2/5-U6-shRNA-MMP2-CMV-EGFP (MMP2-Kd), rAAV2/5-U6-shRNA-MMP9-CMV-EGFP (MMP9-Kd), or rAAV2/5-U6-scramble-CMV-EGFP (scramble) (Fig. 7A). Fourteen days post-injection, mRNA levels of MMP2 and MMP9 were significantly reduced by approximately 70-80% in the ChP of MMP2-Kd and MMP9-Kd mice, respectively (Fig. 7B-C).

Following MOG_{35-55}/CFA immunization, both MMP2-Kd and MMP9-Kd mice showed reduced EAE clinical scores compared to controls (Fig. 7D). On day 14 post-immunization, EAE mice exhibited a significant loss of TJs (ZO-1) in ChP endothelial cells, compared to untreated controls. However, both MMP2-Kd and MMP9-Kd mice demonstrated reduced ZO-1 protein loss, preserving ChP barrier integrity (Fig. 7E-F).

At day 21 post-EAE-induction, analysis of spinal cords tissue revealed decreased MBP loss in both knockdown groups compared to controls (Fig. 7G-H). Additionally, H&E staining showed reduced immune cell infiltration in the knockdown groups (Fig. 7I-J). Consistent with findings in SPAK-Kd mice, both MMP2-Kd and MMP9-Kd mice exhibited decreased distribution of CD68$^+$/Iba1$^+$ cells in the spinal cords, indicating reduced inflammation (Fig. 7K-L). Moreover, reduced CD4$^+$ T cell numbers were observed in both the ChP and spinal cords of

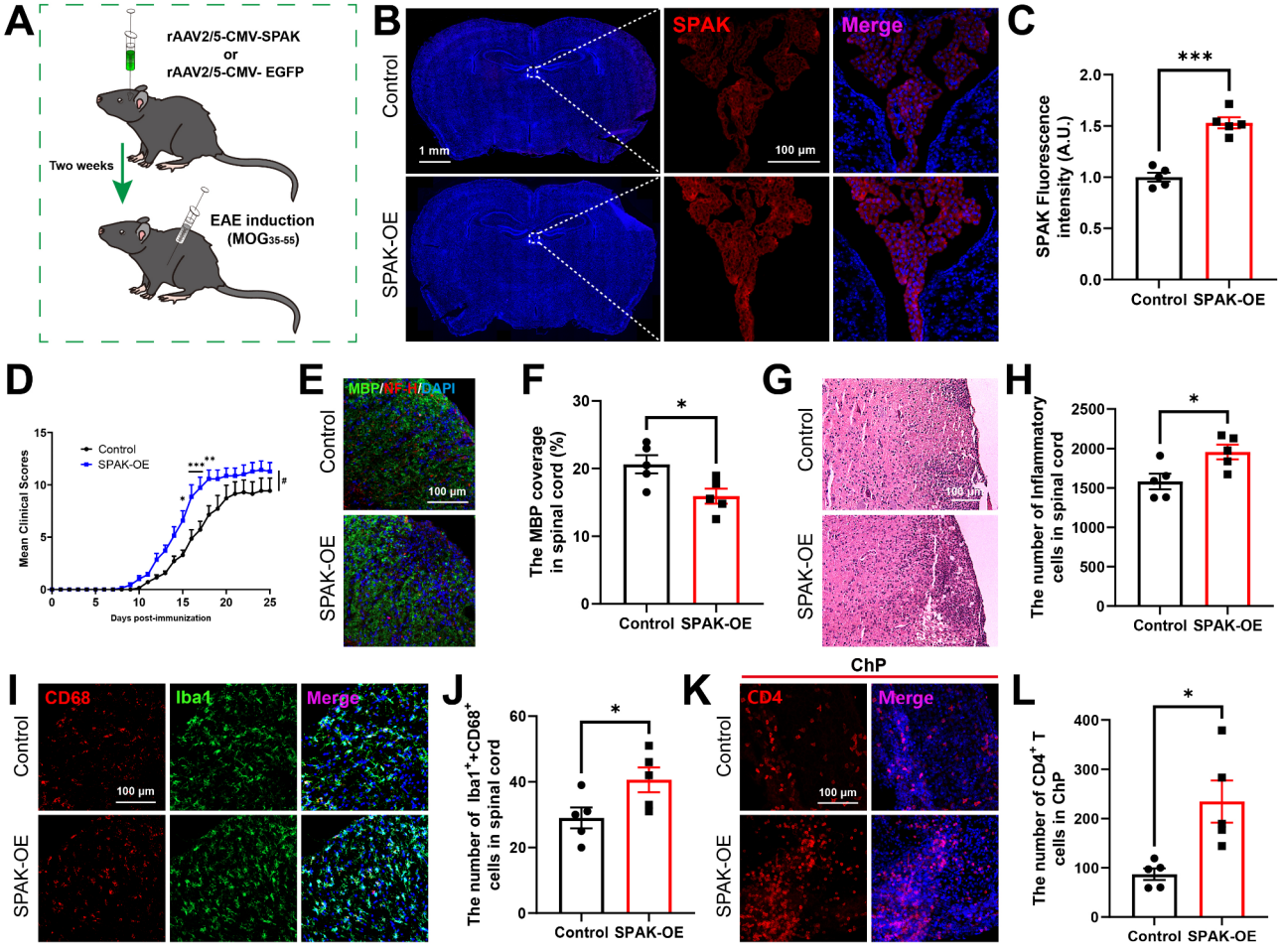

Fig. 4 ChP-Specific SPAK Overexpression Exacerbates EAE Pathology. **A.** Schematic timeline of experimental design for investigating ChP-specific SPAK-OE effects in the EAE model. **B.** Representative immunofluorescence images showing SPAK expression in the ChP 14 days after ICV injection of control or SPAK-OE virus. **C.** Quantification of SPAK fluorescence intensity from panel B ($n = 5$/group). **D.** Clinical disease scores demonstrating enhanced EAE severity in ChP SPAK-OE mice compared to controls ($n = 7$/group). Analysis by two-way RM ANOVA with Sidak's multiple comparisons test. **E.** Representative immunostaining of myelin (MBP) and neuronal (NF-H) markers in spinal cord sections from control and SPAK-OE mice at day 21 post-EAE induction. Scale bar: 100 μm. **F.** Quantification of MBP coverage from panel E ($n = 5$/group). **G.** Representative H&E staining of spinal cord sections at day 14 following EAE induction. Scale bar: 100 μm. **H.** Quantification of immune cell infiltration from panel G. **I.** Representative co-immunostaining of microglial markers Iba1 and CD68 in spinal cords at day 14 post-EAE induction. Scale bar: 100 μm. **J.** Quantification of $Iba1^+/CD68^+$ double-positive microglia from panel I ($n = 5$/group). **K.** Representative CD4 immunostaining in ChP tissue at day 14 post-EAE induction from control and SPAK-OE mice. Scale bar: 100 μm. **L.** Quantification of $CD4^+$ T cells from panel K ($n = 5$/group). Statistical analyses performed using unpaired t-test unless otherwise specified. Data are presented as mean ± SEM. $^{\#}P < 0.05$, $^{*}P < 0.05$, $^{**}P < 0.01$, $^{***}P < 0.001$. ChP: choroid plexus

MMP2-Kd and MMP9-Kd mice compared to controls (Fig. 7M-P).

SPAK-NKCC1 inhibitors protect against EAE pathology

To assess the therapeutic potential of SPAK-NKCC1 inhibitors for MS treatment, we administered daily intraperitoneal injections of the SPAK inhibitor ZT-1a or vehicle following EAE induction. ZT-1a treatment significantly reduced EAE clinical scores (Fig. 8A-B) and attenuated myelin loss, as measured by MBP staining (Fig. 8C-D). Additionally, ZT-1a reduced both immune cell infiltration (Fig. 8E-F) and inflammation in spinal cords, as evidenced by decreased $CD68^+/Iba1^+$ double-positive cells (Fig. 8G-L).

Immunostaining revealed that ZT-1a treatment reduced $CD4^+$ T cell infiltration in both the ChP (Fig. 8M-N) and spinal cords (Fig. 8O-P). FCM analysis at day 14 post-EAE induction confirmed that ZT-1a significantly protected against the invasion of $CD4^+$ T cells, including both the $Th1^+$ and $Th17^+$ subsets (Fig. 9A-H).

Bumetanide, a Food and Drug Administration (FDA)-approved NKCC1 inhibitor used for treating edematous conditions, showed no improvement in EAE clinical scores when administered intraperitoneally (Fig. 10A), likely due to its poor CNS penetration [13]. To overcome

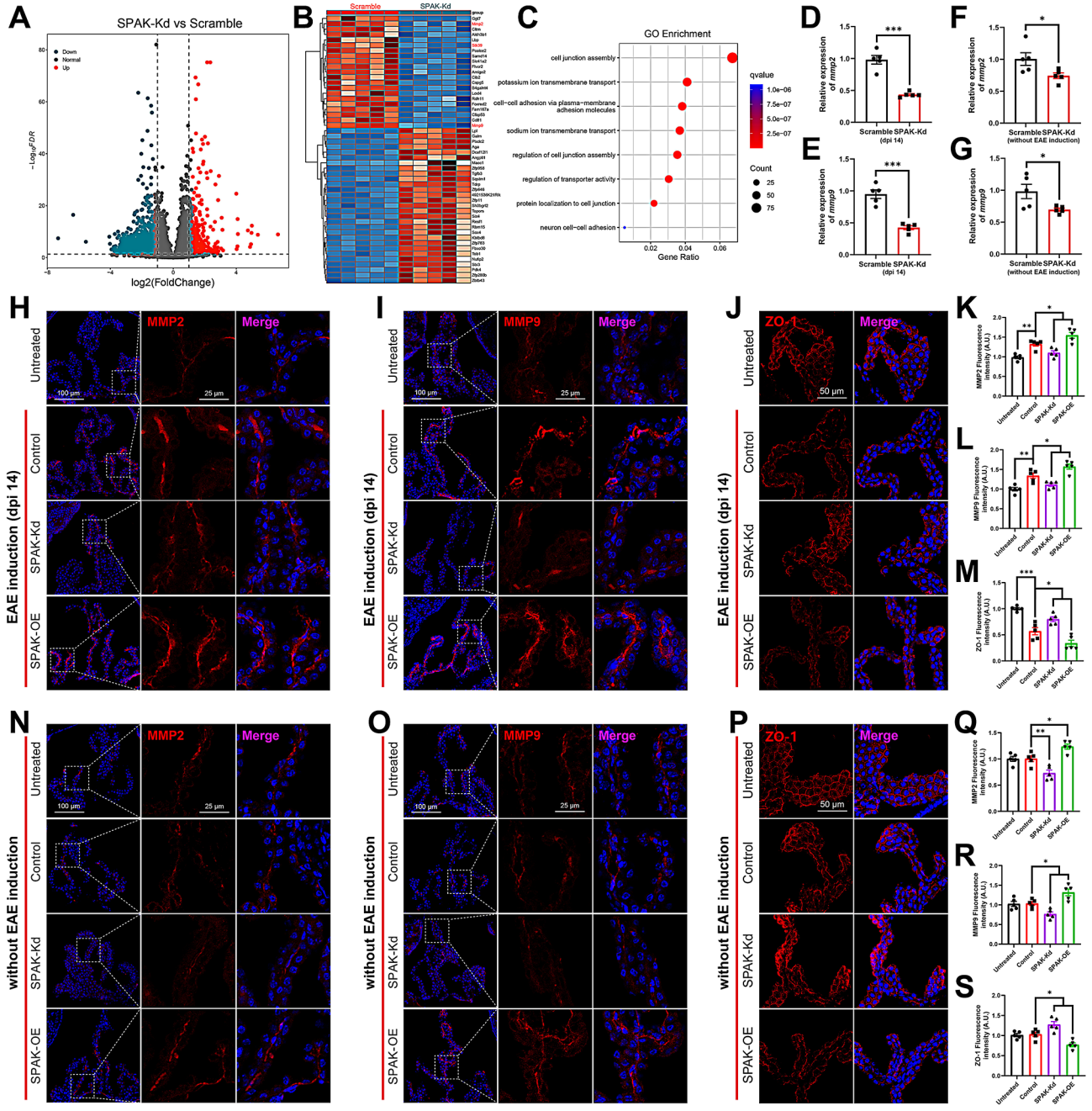

Fig. 5 SPAK Signaling Modulates MMP and ZO-1 Expression in ChP Epithelium. **A.** Volcano plot analysis of DEGs in the ChP following SPAK-Kd at day 14 post-EAE induction, determined by bulk RNA-seq ($n = 5$/group). **B.** Heatmap depicting the Top 50 DEGs identified from RNA-seq analysis. **C.** GO enrichment analysis of identified DEGs. **D-E.** The qPCR validation of RNA-seq results showing expression of *mmp2* (**D**) and *mmp9* (**E**) at day 14 post-EAE induction ($n = 5$/group). **F-G.** The qPCR analysis of *mmp2* (**F**) and *mmp9* (**G**) expression in the ChP of non-EAE mice 14 days after SPAK-Kd or scramble virus injection ($n = 5$/group). **H-J.** Representative immunofluorescence images showing expression of MMP2 (**H**), MMP9 (**I**), and ZO-1 (**J**) in the ChP at day 14 post-EAE induction across treatment groups: untreated, control, SPAK-Kd, and SPAK-OE. Scale bars: 100 μm, 50 μm, 25 μm. **K-M.** Quantification of fluorescence intensity for MMP2 (**K**), MMP9 (**L**), and ZO-1 (**M**) from panels **H**-**J**. **N-P.** Representative immunofluorescence images showing expressions of MMP2 (**N**), MMP9 (**O**), and ZO-1 (**P**) in the ChP of non-EAE mice at day 14 across treatment groups. Scale bars: 100 μm, 50 μm, 25 μm. **Q-S.** Quantitative analysis of fluorescence intensity for MMP2 (**Q**), MMP9 (**R**), and ZO-1 (**S**) from panels N-P ($n = 5$/group). Statistical analyses performed using unpaired t-test or one-way ANOVA with Tukey's multiple comparisons test as indicated. Data are presented as mean ± SEM. * $P < 0.05$, ** $P < 0.01$, *** $P < 0.001$. ChP: choroid plexus; dpi: day post immunization

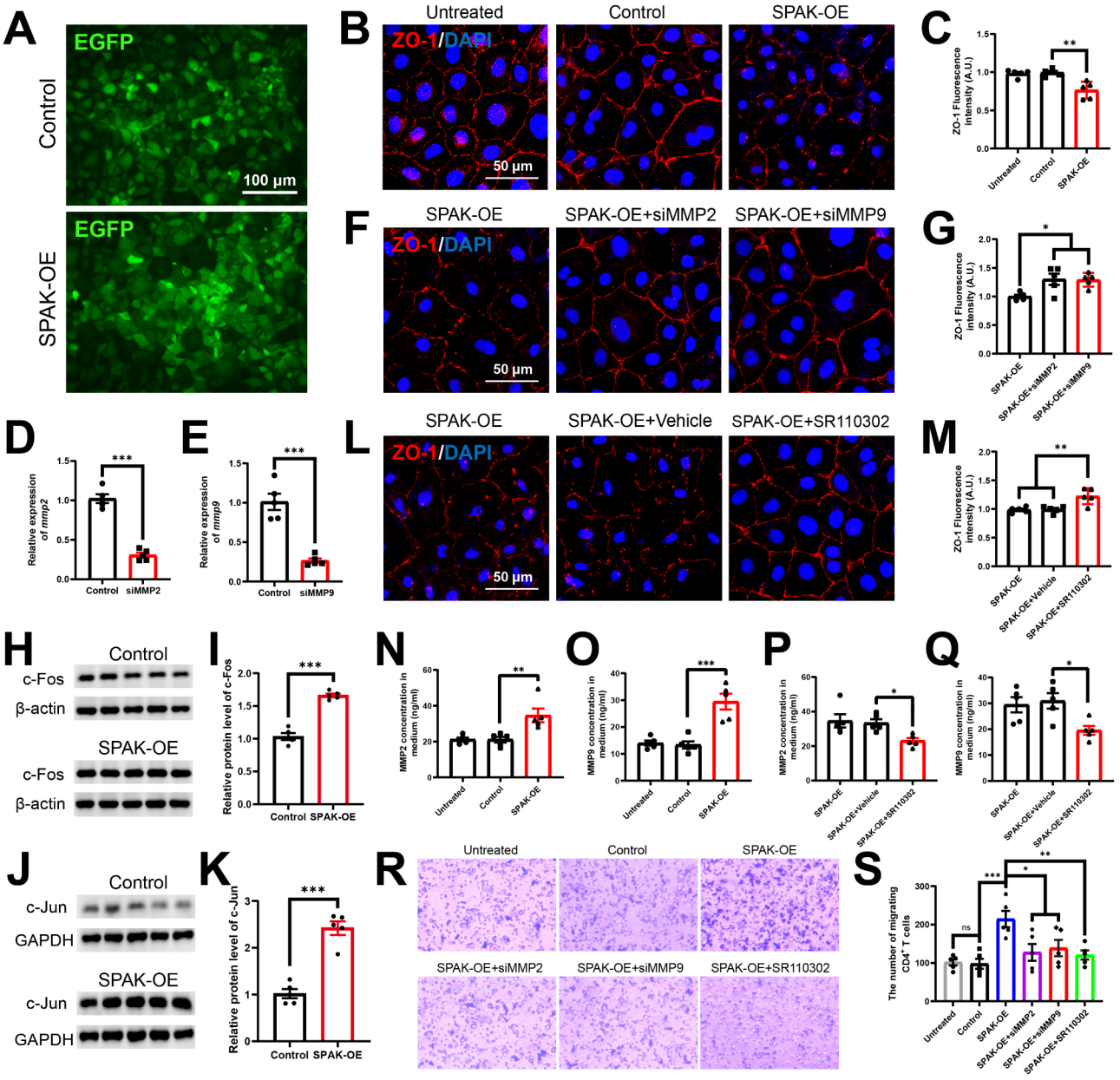

Fig. 6 SPAK Modulates ChP Barrier Integrity via the AP-1-MMP2/9-ZO1 Signaling Axis. **A.** Representative EGFP fluorescence images confirming stable expression of SPAK-OE or empty vector control in Z310 cells. Scale bar: 100 μm. **B.** Representative immunofluorescence images showing reduced ZO-1 expression in SPAK-OE Z310 cells. Scale bar: 50 μm. **C.** Quantification of ZO-1 fluorescence intensity ($n = 5$/group). **D-E.** The qPCR analysis confirming knockdown efficiency of *mmp2* (**D**) and *mmp9* (**E**) in siRNA-transfected Z310 cells ($n = 5$/group). **F.** Representative immunofluorescence images showing partial restoration of ZO-1 expression following MMP2/9 knockdown. Scale bar: 50 μm. **G.** Quantification of ZO-1 fluorescence intensity ($n = 5$/group). **H-K.** Western blot analysis of AP-1 components in control and SPAK-OE Z310 cells: Representative immunoblots (**H**) and quantification of c-Fos (**I**); Representative immunoblots (**J**) and quantification of c-Jun (**K**) ($n = 5$/group). **L.** Representative immunofluorescence images showing partial rescue of ZO-1 expression in SPAK-OE cells treated with AP-1 inhibitor SR110302 (1 μM). Scale bar: 50 μm. **M.** Quantification of ZO-1 fluorescence intensity ($n = 5$/group). **N-Q.** ELISA quantification of secreted MMPs: MMP2 (**N**) and MMP9 (**O**) levels in control vs. SPAK-OE cell; MMP2 (**P**) and MMP9 (**Q**) levels following AP-1 inhibitor treatment ($n = 5$/group). **R-S.** Quantification of T cell migration in transwell assays showing enhanced migration with SPAK-OE and partial rescue by MMP2/9 siRNAs and SR110302 treatment ($n = 5$/group). Statistical analyses performed using unpaired t-test or one-way ANOVA with Tukey's multiple comparisons test as indicated. Data are presented as mean ± SEM. ns: non-significant, * $P < 0.05$, ** $P < 0.01$, *** $P < 0.001$. ChP: choroid plexus

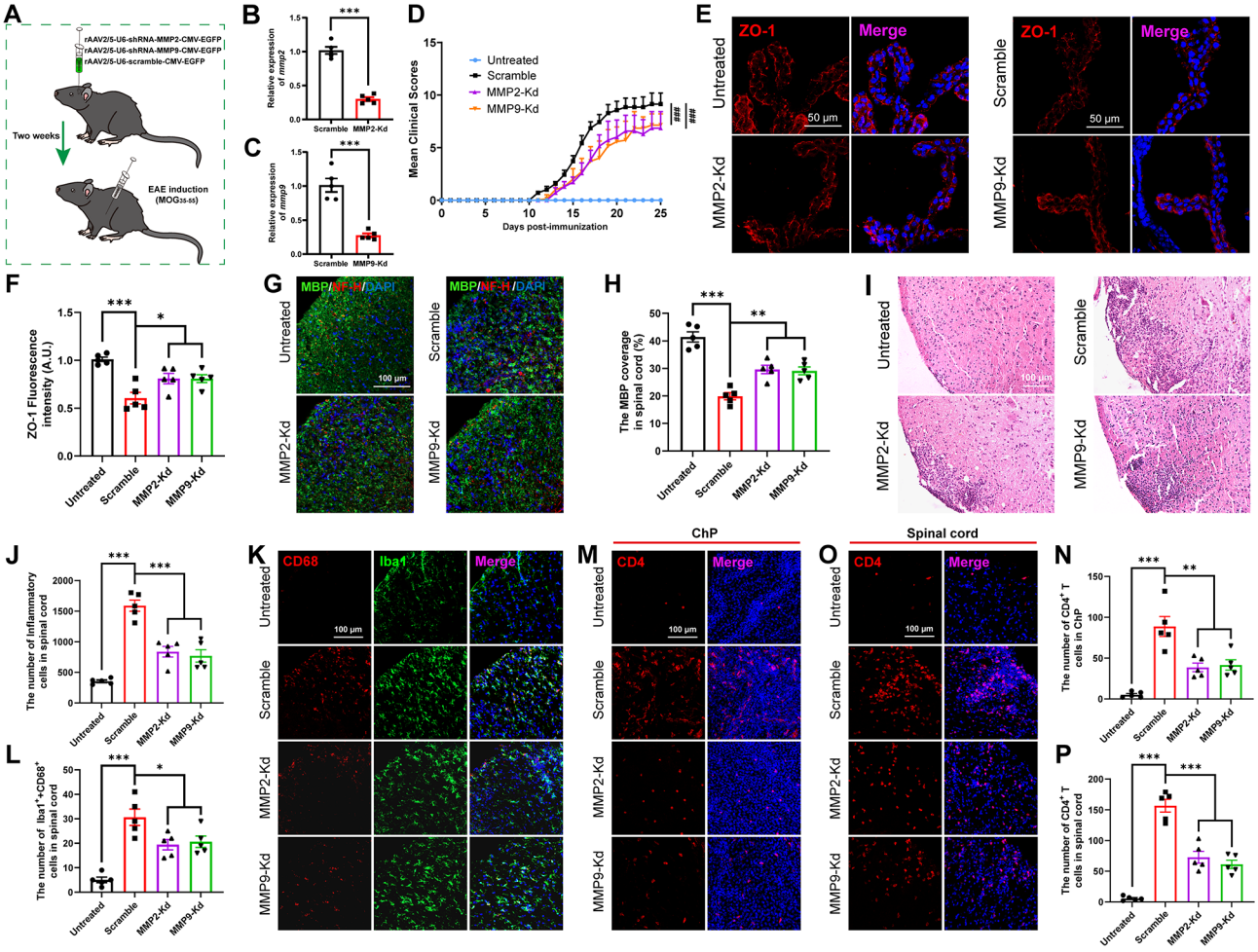

Fig. 7 ChP-Specific Knockdown of MMP2/9 Attenuates EAE Pathology. **A.** Schematic timeline of the experimental design for evaluating the effects of ChP-specific knockdown of MMP2 (MMP2-Kd) and MMP9 (MMP9-Kd) in the EAE model. **B-C.** The qPCR analysis confirmed significant reductions in *mmp2* (**B**) and *mmp9* (**C**) mRNA expression levels in the ChP of MMP2-Kd and MMP9-Kd mice, respectively, 14 days following ICV injection ($n = 5$/group). Statistical analysis by unpaired t-test. **D.** Clinical disease scores showing reduced EAE severity in MMP2-Kd and MMP9-Kd mice compared to controls ($n = 7$/group). Statistical analysis by two-way RM ANOVA with Sidak's multiple comparisons test. **E.** Representative immunofluorescence images showing ZO-1 expression in the ChP at day 14 post-EAE induction across treatment groups: untreated, scramble, MMP2-Kd, and MMP9-Kd. Scale bar: 50 μm. **F.** Quantification of ZO-1 fluorescence intensity from panel E ($n = 5$/group). Statistical analysis by one-way ANOVA with Tukey's multiple comparisons test. **G.** Representative immunostaining of myelin (MBP) and neuronal (NF-H) markers in spinal cord sections from untreated, scramble, MMP2-Kd, and MMP-Kd mice at day 21 post-EAE induction. Scale bar: 100 μm. **H**. Quantification of MBP coverage in spinal cords from panel G ($n = 5$/group). Statistical analysis by one-way ANOVA with Tukey's multiple comparisons test. **I.** Representative H&E staining of spinal cord sections at day 14 post-EAE induction across treatment groups: untreated, scramble, MMP2-Kd, and MMP9-Kd. Scale bar: 100 μm. **J.** Quantification of immune cell infiltration identified in panel I ($n = 5$/group). One-way ANOVA with Tukey's multiple comparisons test. **K.** Representative co-immunostaining of microglial markers Iba1 and CD68 in spinal cord sections at day 14 post-EAE induction across treatment groups. Scale bar: 100 μm. **L.** Quantification of $Iba1^+/CD68^+$ double-positive microglial cells from panel K ($n = 5$/group). One-way ANOVA with Tukey's multiple comparisons test. **M.** CD4 immunostaining in ChP tissues at day 14 post-EAE induction across treatment groups: untreated, scramble, MMP2-Kd, and MMP9-Kd. Scale bar: 100 μm. **N.** Quantification of $CD4^+$ T cells from panel M ($n = 5$/group). One-way ANOVA with Tukey's multiple comparisons test. **O.** Representative CD4 immunostaining in spinal cord sections at day 14 post-EAE induction across treatment groups: untreated, control, MMP2-Kd, and MMP9-Kd. Scale bar: 100 μm. **P.** Quantification of $CD4^+$ T cells in spinal cords from panel O ($n = 5$/group). One-way ANOVA with Tukey's multiple comparisons test. Data are presented as mean ± SEM. $^{###}P < 0.001$, * $P < 0.05$, ** $P < 0.01$, *** $P < 0.001$. ChP: choroid plexus

this limitation, we implemented direct ICV delivery of bumetanide via a daily micropump following EAE induction (Fig. 10B). This CNS-targeted delivery approach significantly improved EAE clinical scores (Fig. 10C), enhanced myelin preservation as measured by MBP staining (Fig. 10D-E), and reduced T cell infiltration into the CNS via the ChP (Fig. 10F-G).

Given that T cell infiltration primarily occurs between EAE onset and peak clinical scores [10], we evaluated ICV bumetanide administration during days 8-14 post-EAE induction. This targeted treatment window proved

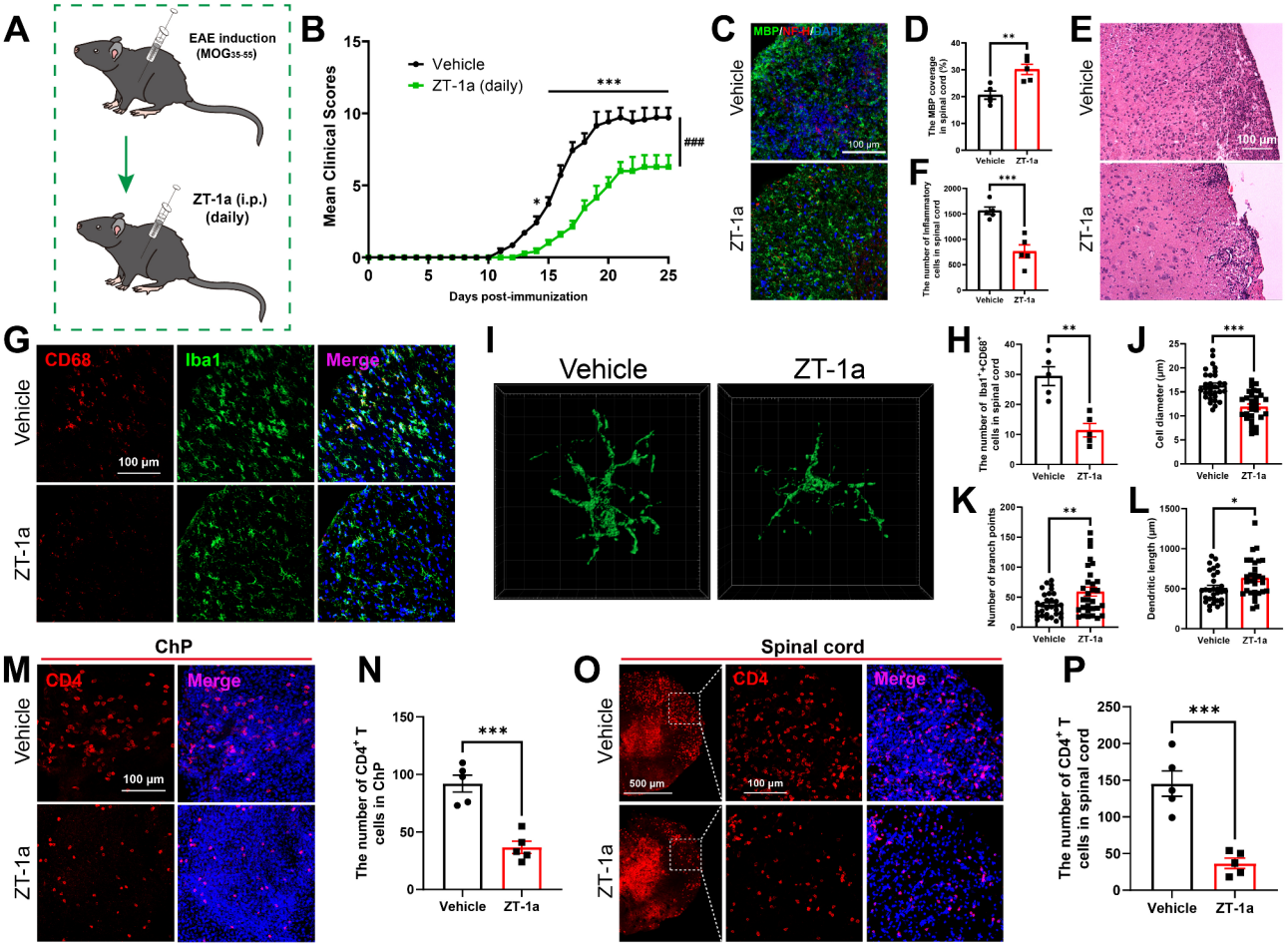

Fig. 8 SPAK Inhibition by ZT-1a Demonstrates Protective Effects against EAE Pathology. **A.** Schematic timeline of experimental design for investigating ZT-1a treatment effects in the EAE model. **B.** Clinical disease scores demonstrating reduced EAE severity in ZT-1a-treated mice compared to vehicle controls ($n = 7$/group). Analysis by two-way RM ANOVA with Sidak's multiple comparisons test. **C.** Representative immunostaining of myelin (MBP) and neuronal (NF-H) markers in spinal cord sections from vehicle- and ZT-1a-treate mice at day 21 following EAE induction. Scale bar: 100 μm. **D.** Quantification of MBP coverage from panel C ($n = 5$/group). **E.** H&E staining of spinal cord sections at day 14 post-EAE induction. Scale bar: 100 μm. **F.** Quantification of immune cell infiltration from panel E ($n = 5$/group). **G.** Representative co-immunostaining of microglial markers Iba1 and CD68 in spinal cords at day 14 following EAE induction. Scale bar: 100 μm. **H.** Quantification of $Iba1^+/CD68^+$ double-positive microglia from panel G ($n = 5$/group). **I.** Three-dimensional reconstruction of microglial morphology in spinal cords at day 14 post-EAE induction. **J-L.** Morphometric analysis of microglia: cell diameter (**J**), branch points (**K**), and dendritic length (**L**) from panel I ($n = 30$ cells/group). **M.** Representative CD4 immunostaining in ChP tissues at day 14 following EAE induction. Scale bar: 100 μm. **N.** Quantification of $CD4^+$ T cells from panel M ($n = 5$/group). **O.** Representative CD4 immunostaining in spinal cords at day 14 post-EAE induction. Scale bar: 100 μm. **P.** Quantification of $CD4^+$ T cells from panel O ($n = 5$/group). Statistical analyses performed using unpaired t-test unless otherwise specified. Data are presented as mean ± SEM. $^{###}P < 0.001$, $^{*}P < 0.05$, $^{**}P < 0.01$, $^{***}P < 0.001$. i.p.: intraperitoneal, ChP: choroid plexus

effective, as evidenced by reduced EAE clinical scores (Fig. 10H), decreased myelin loss (Fig. 10I-J), and reduced $CD4^+$ T cell infiltration through the ChP (Fig. 10K-L).

Discussion

Our study identifies SPAK signaling in the ChP as a promising therapeutic target for MS, supported by five key findings: (1) During EAE pathology, SPAK expression was selectively elevated in the ChP compared to other brain regions. (2) ChP-specific SPAK manipulation directly influenced EAE severity, with SPAK-Kd ameliorating EAE pathology and SPAK-OE exacerbating brain damage. (3) SPAK regulated T cell infiltration through the ChP via the AP-1-MMP2/9-TJs in EAE. (4) Knockdown of MMP2 or MMP9 in ChP prevented T cell infiltration and alleviated brain damage. (5) SPAK-NKCC1 inhibitors (ZT-1a and bumetanide) demonstrated significant therapeutic efficacy in reducing EAE symptoms.

SPAK signaling in ChP epithelium is a critical mediator of barrier integrity

Previous studies have demonstrated SPAK-NKCC1 upregulation in ChP, with SPAK-NKCC1 antagonists showing protective effects on ChP barrier integrity in stroke [14]. However, the systemic distribution of these antagonists made it challenging to identify specific

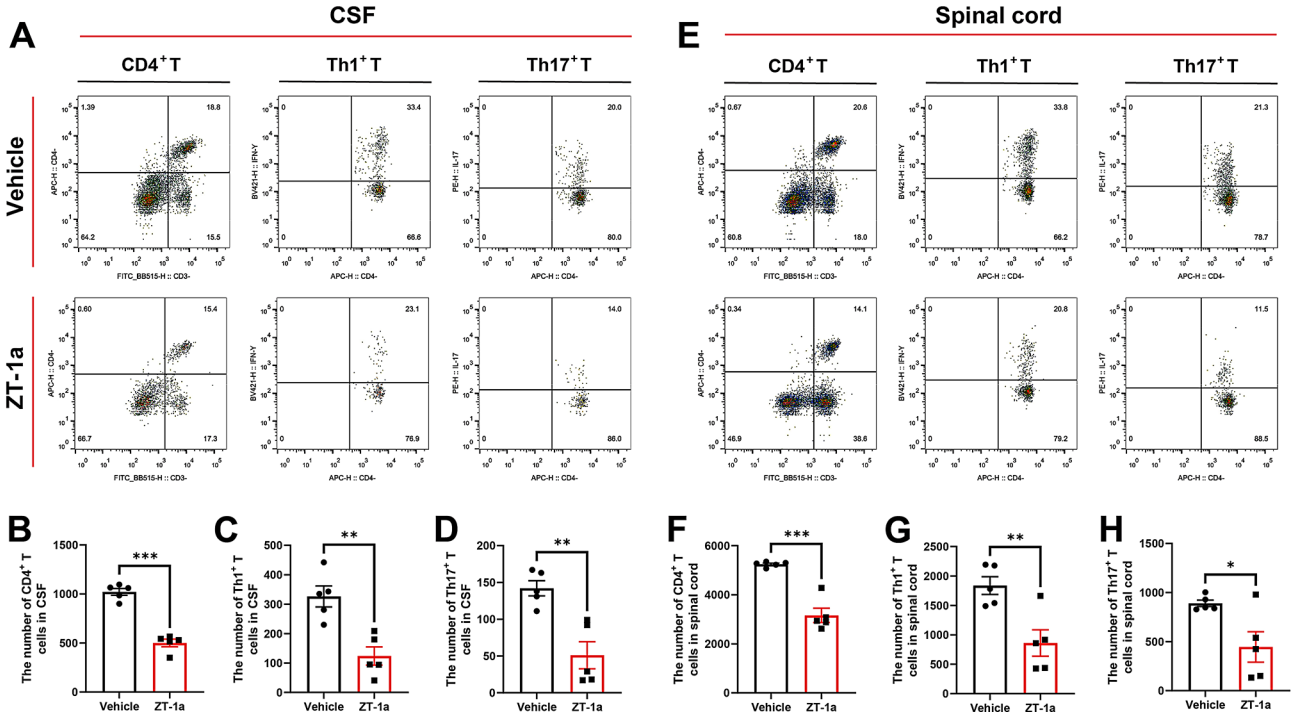

Fig. 9 SPAK Inhibition by ZT-1a Reduces CNS Infiltration of CD4$^+$ T Cell Subsets. **A.** Representative FCM plots showing CD4$^+$, Th1$^+$, and Th17$^+$ T cell populations in CSF at day 14 post-EAE induction in vehicle- and ZT-1a-treated mice. **B-D.** Quantitative analysis of CSF FCM data demonstrating reduced infiltration of CD4$^+$ (**B**), Th1$^+$ (**C**), and Th17$^+$ (**D**) T cells following ZT-1a treatment ($n = 5$/group). **E.** FCM analysis of CD4$^+$, Th1$^+$, and Th17$^+$ T cell populations in spinal cords at day 14 post-EAE induction in vehicle- and ZT-1a-treated mice. **F-H.** Quantitative analysis of spinal cords FCM data demonstrating reduced infiltration of CD4$^+$ (**F**), Th1$^+$ (**G**), and Th17$^+$ (**H**) T cells following ZT-1a treatment ($n = 5$/group). Statistical analyses performed using unpaired t-test. Data are presented as mean ± SEM. * $P < 0.05$, ** $P < 0.01$, *** $P < 0.001$. ChP: choroid plexus

therapeutic targets. Furthermore, contradictory findings reported that SPAK-Kd did not affect immune cell infiltration in hemorrhagic hydrocephalus [12], raising questions about SPAK's role in barrier maintenance.

Using the EAE model, which is optimal for studying immune cell infiltration across the ChP, we performed ChP-specific SPAK manipulation to establish causality. Our findings revealed that under EAE conditions, SPAK-Kd reduced T cell infiltration across the ChP and partially restored ChP barrier integrity, as evidenced by increased ZO-1 levels. Under physiological conditions, SPAK-Kd increased ZO-1 expression, whereas SPAK-OE reduced ZO-1 expression and distribution, and enhanced T cell migration, both in vivo and in vitro. However, it is important to note that SPAK-OE in the ChP alone did not cause demyelination or immune infiltration in the absence of MOG/CFA induction.

TNF-α, a critical pro-inflammatory cytokine secreted by CD4$^+$ T cells, has been reported to induce SPAK expression [26]. In our previous study, we observed that ChP barrier impairment and the aggregation of T cells at the ChP began at day 8 post-EAE induction [10]. Here, we found the increased protein levels of SPAK and p-SPAK occurred during the same time window. A possible molecular mechanism is that infiltrating CD4$^+$ T cells activate SPAK by secreting TNF-α, and the activated SPAK signaling disrupts the ChP barrier integrity, leading to immune infiltration and injury in EAE pathology.

Of note, previous studies [14] and our findings showed that the protein distribution of SPAK in vitro (in ChP cell line or primary ChP epithelium) differs from the pattern observed in ChP tissue. in vivo, SPAK also has a certain amount of accumulation in the cytoplasm of ChP epithelial cells under pathological conditions [14]. This suggests that SPAK, as a scaffold protein, may regulate other cellular processes by interacting with cytoplasmic proteins. However, unlike in vivo conditions, the cell culture environment may disturb the polar distribution of proteins in cells [27]. Therefore, 3D cell culture models are more suitable for studying functions related to protein polarity distributions. Despite this, we demonstrated that SPAK regulates ChP barrier function both in vivo and in vitro, suggesting that the polar distribution of SPAK protein may not be essential for regulating ChP barrier integrity. These findings establish SPAK as a critical regulator of ChP barrier integrity, providing direct evidence for its role independent of the disease state.

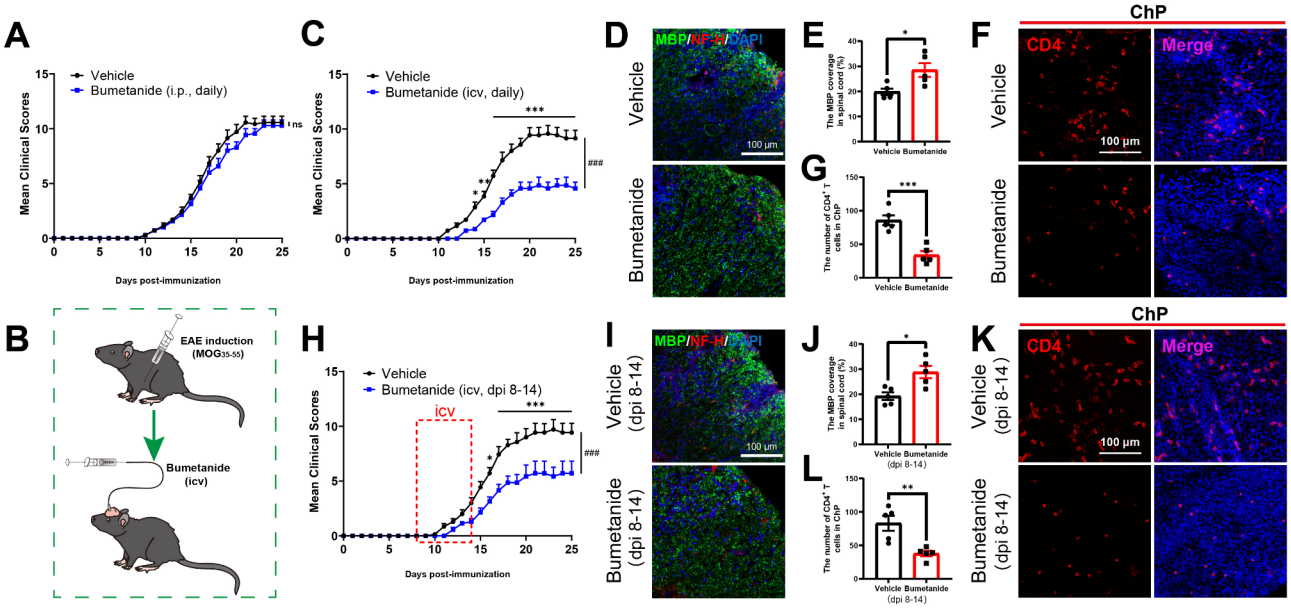

Fig. 10 ICV Administration of Bumetanide Ameliorates EAE Pathology. **A.** Clinical disease scores showing no effect of intraperitoneal bumetanide administration ($n=7$/group). Analysis by two-way repeated measures ANOVA with Sidak's multiple comparisons test. **B.** Schematic timeline of experimental design for evaluating bumetanide treatment effects in the EAE model. **C.** Clinical scores demonstrated reduced EAE severity with daily ICV bumetanide administration ($n=7$/group). Two-way RM ANOVA with Sidak's multiple comparisons test. **D.** Representative immunostaining of MBP in spinal cord sections from control and bumetanide-treated mice. Scale bar: 100 μm. **E.** Quantification of MBP coverage ($n=5$/group). Unpaired t-test. **F.** Representative CD4 immunostaining in ChP tissue at day 14 post-EAE induction. Scale bar: 100 μm. **G.** Quantification of $CD4^+$ T cells ($n=5$/group). Unpaired t-test. **H.** Clinical disease scores showing reduced EAE severity with ICV bumetanide administration during days 8-14 post-EAE induction ($n=7$/group). Two-way RM ANOVA with Sidak's multiple comparisons test. **I-J.** ICV injection of bumetanide administered during days 8-14 post-EAE induction significantly reduces MBP loss in the spinal cords compared to the control group ($n=5$/group). Scale bar: 100 μm. Unpaired t-test. **K-L.** ICV injection of bumetanide during days 8-14 post-EAE induction decreases $CD4^+$ T cell infiltration in the ChP during the same time ($n=5$/group). Scale bar: 100 μm. Unpaired t-test. Data are presented as mean ± SEM. ns: non-significant, $^{###}P<0.001$, * $P<0.05$, ** $P<0.01$, *** $P<0.001$. i.p.: intraperitoneal, ChP: choroid plexus; dpi: day post immunization. Note: CD4 immunostaining was performed on isolated ChP tissues rather than brain slices

SPAK's role in MS/EAE pathology via the AP-1-MMP2/9-TJs axis

The ChP plays a pivotal role in MS, with increased ChP volume in MS patients serving as a potential diagnostic biomarker to distinguish MS from similar conditions. SPAK-NKCC1 signaling is well-established as a key regulator of cellular volume and swelling dynamics [22]. Our observation of progressively increasing SPAK-NKCC1 phosphorylation levels during EAE pathology suggests that dysregulated SPAK-NKCC1 activity may contribute to the enlarged ChP volume observed in MS patients. Furthermore, our experimental findings that SPAK-OE enhances T cell migration provide a mechanistic link between increased ChP volume and immune cell infiltration in MS. These results suggest that ChP enlargement is not merely a structural change but may actively facilitate disease progression by promoting immune cell trafficking.

MMPs are elevated in both the CSF and lesion sites of MS patients, where they compromise the blood-brain barrier (BBB) by degrading TJs and matrix components [28, 29]. Recent studies In ChP tissue demonstrated that chemotherapy-induced MMP9 expression contributes to claudin-6 downregulation, while MMP9-Kd reverses this effect [30]. However, the specific contribution of MMPs in MS/EAE has remained uncertain. Our research provides compelling evidence that ChP-specific knockdown of either MMP2 or MMP9 significantly attenuates EAE progression, characterized by reduced immune cell infiltration and restored ChP barrier integrity. These findings directly support the critical role of MMP2/9 in facilitating immune cell invasion across the ChP during EAE pathogenesis.

The transcription factor AP-1, known to regulate MMP2/9 expression [31, 32], is activated by SPAK during T cell activation [25]. Our studies revealed that SPAK similarly activates AP-1 in ChP epithelium, leading to increased MMP2/9 expression. Importantly, our rescue experiments demonstrated that both AP-1 inhibition and siRNA-mediated MMP2/9 knockdown could reverse the barrier dysfunction caused by SPAK-OE. These findings establish a clear mechanistic pathway whereby ChP SPAK regulates T cell invasion via the AP-1-MMP2/9-TJs axis in the EAE model. In contrast, NF-κB is also a transcriptional regulator of MMPs. While it is reported that SPAK inhibitors reduce NF-κB phosphorylation

in a stroke model [14], NF-κB is often considered an upstream mediator that regulates SPAK transcription [26, 33].

Additionally, SPAK phosphorylates NKCC1 by interacting with its N-terminal cytoplasmic domain [34]. This SPAK-NKCC1 signaling is thought to disrupt the cytoskeletal structure of cells, leading to cell swelling, apoptosis, and ultimately BBB damage [35]. Inhibition of NKCC1 has been shown to reduce BBB disruption and MMP9 secretion in traumatic brain injury [36]. In this study, we found that SPAK activates AP-1, which regulates the secretion of MMP2 and MMP9 in the ChP. However, the precise molecular mechanism by which NKCC1 regulates AP-1-MMP2/9 expression remains unclear. Combining prior findings that NKCC1 may regulate TJ expression via a Cl^--sensing mechanism in HT29 cells [37], we hypothesize that changes in ion concentrations induced by SPAK-NKCC1 signaling mediate the activation of AP-1, which further regulates the MMP-TJs axis in ChP epithelial cells.

SPAK-NKCC1 inhibitors are promising therapeutic candidates for MS treatment

Our investigation highlights the significant therapeutic potential of SPAK-NKCC1 inhibitors for EAE treatment. The administration of ZT-1a effectively protected mice against CNS T cell infiltration and reduced demyelination. The preferential expression of SPAK in the ChP, compared to other brain regions, suggests that the ChP may be the primary target for ZT-1a's therapeutic action. This finding aligns with previous studies showing ZT-1a's efficacy (via intraperitoneal injection) in treating various CNS disorders, including stroke, vascular dementia, and hydrocephalus [14, 15, 38]. Despite reports of ZT-1a's limited brain penetration [38], its consistent therapeutic effects across multiple CNS disorders suggest that intraperitoneal administration of ZT-1a successfully reaches the ChP, as evidenced by increased SPAK and p-SPAK levels in ChP epithelium, effectively blocking SPAK-NKCC1 signaling.

In contrast to ZT-1a, bumetanide is an FDA-approved drug, making it particularly appealing for therapeutic applications. Our research revealed that while intraperitoneal bumetanide administration (5 mg/kg) showed no significant effect on EAE pathology, ICV delivery of bumetanide exhibited marked therapeutic benefits. This differential response aligns with well-documented evidence of bumetanide's poor BBB penetration [13, 16]. Previous studies have shown that direct CNS delivery of bumetanide, via ICV or intrathecal injection, provides therapeutic benefits in conditions such as hydrocephalus and spinal cord injury [16, 39]. This delivery method effectively bypasses challenges associated with high plasma-protein binding and potential brain-tissue binding [40]. Our findings are consistent with this approach, showing that ICV-administered bumetanide reduced EAE pathology, which correlated with increased p-NKCC1 levels in the ChP epithelium during EAE progression.

Interestingly, some studies have reported therapeutic success with high-dose intraperitoneal bumetanide administration in other neurological conditions, including stroke (10 mg/kg) [14] and traumatic brain injury (25 mg/kg) [41]. These varying results suggest that bumetanide's bioavailability may be disease-dependent, potentially influenced by the degree of BBB disruption, and dose-dependent. This complexity underscores the need for more comprehensive pharmacokinetic studies to optimize bumetanide's therapeutic application across different neurological conditions.

Moreover, the mechanism of RNA interference inherently limits its ability to achieve complete transcriptional inhibition. To overcome this, knockdown of SPAK in $SPAK^{flox/flox}$ mice via ICV injection of recombinant TAT-Cre would enable stronger transcriptional inhibition of SPAK, providing a more robust and accurate evaluation of the ChP-SPAK contribution to EAE/MS pathology. Furthermore, it would be valuable to investigate the synergistic effects of combining existing DMTs with the inhibition of ChP-SPAK signaling in future studies. Such research could further strengthen the case for SPAK as a therapeutic target in MS treatment.

Limitations of the study

It is important to acknowledge that no existing experimental model fully recapitulates the entire spectrum of MS pathology, given its complexity. The MOG_{35-55}-induced EAE model, which is primarily utilized in this study, is widely regarded as a model of relapsing-remitting MS [42, 43]. However, this model does not adequately represent the progressive forms of MS, including secondary-progressive disability, axonal degeneration, and remyelination. Moreover, the MOG_{35-55} model predominantly focuses on T lymphocyte activation and infiltration, while growing evidence highlights the critical role of B cells in MS pathogenesis [44] - a factor that is not fully addressed by this model. To comprehensively evaluate the therapeutic potential of targeting SPAK-NKCC1 signaling in MS treatment, further research utilizing additional MS models is necessary. These models should better capture the diverse pathological features of MS, including progressive forms and B cell-mediated mechanisms, to provide a more complete understanding of the effectiveness of SPAK-NKCC1 inhibition.

Conclusions

This study identifies SPAK as a critical regulator of ChP barrier integrity in the pathogenesis of EAE and MS. SPAK activation compromises the ChP barrier via the AP-1-MMP2/9-TJ axis, promoting T cell infiltration into the CNS and driving immune-mediated damage. Our findings demonstrate that pharmacological inhibition of the SPAK-NKCC1 pathway, through agents such as ZT-1a or bumetanide, effectively preserves ChP barrier function, offering a promising therapeutic approach for MS.

Abbreviations

DMTs	Disease-modifying therapies
MS	Multiple sclerosis
ChP	Choroid plexus
SPAK	Ste20-related proline/alanine-rich kinase
EAE	Experimental autoimmune encephalomyelitis
CNS	Central nervous system
CSF	Cerebrospinal fluid
BCSFB	Blood-cerebrospinal fluid barrier
NKCC1	Na-K-2Cl cotransporter-1
p-SPAK	phosphorylated SPAK
p-NKCC1	phosphorylated NKCC1
Kd	Knockdown
OE	Overexpression
rAAV2/5	Recombinant adeno-associated virus 2/5
MBP	Myelin basic protein
MMP	Matrix metalloproteinase
ZO-1	Zonula occludens-1
TJs	Tight junctions
BBB	Blood-brain barrier
AP-1	Activator protein-1
dpi	Day post-immunization
ICV	Intracerebroventricular
FDA	Food and Drug Administration
GO	Gene Ontology
KEGG	Kyoto Encyclopedia of Genes and Genomes
MOG	Myelin oligodendrocyte glycoprotein
RM	Repeated measures
CFA	Complete Freund's adjuvant
H&E	Hematoxylin-Eosin
FCM	Flow Cytometry
MOI	Multiplicity of Infection
ELISA	Enzyme-linked Immunosorbent Assay
RNA-seq	RNA sequencing
PFA	Paraformaldehyde
qPCR	Quantitative real-time PCR
TBST	Tris-buffered saline containing 0.1% Tween 20
DAPI	4',6-diamidino-2-phenylindole
DEGs	Differentially expressed genes

Supplementary Information

The online version contains supplementary material available at https://doi.org/10.1186/s12974-025-03407-5.

Supplementary Material 1

Supplementary Material 2

Supplementary Material 3

Supplementary Material 4

Acknowledgements

Not applicable.

Author contributions

W.Z., Z.L., and Y.Z. conceived and designed the study. W.Z., C.Q., Y.W., X.L., and C.Z. performed the experiments. Y.G., Y.Q., J.H., G.X., and S.X. analyzed the data. W.Z. wrote the manuscript. All authors reviewed and approved the final manuscript.

Funding

This study was supported by grants from the Natural Science Foundation of Zhejiang Province (Grant No. LMS25H090008), the National Natural Science Foundation of China (Grant No. 31800903), the Medical and Health Research Project of Zhejiang Province (Grant No. 2024KY303), the Ningbo Major Research and Development Plan Project (Grant No. 2023Z196 and 2023Z173), the Neurology Department of the National Key Clinical Specialty Construction Project, the Ningbo Medical and Health Brand Discipline (Grant No. PPXK2024-01), and the PhD start-up funding from Lihuili Hospital (Grant No. 2024BSKY-ZW).

Data availability

The datasets generated and analyzed during this study are available from the corresponding author (W.Z.) upon reasonable request.

Declarations

Ethics approval and consent to participate

The study (ethics protocol number: HT-2024-LWFB-0022) was approved by the Animal Care and Use Committee of Zhejiang Huitong Test & Evaluation Technology Group.

Consent for publication

Not applicable.

Competing interests

The authors declare no competing interests.

Author details

[1]Department of Neurology, Ningbo Medical Center Lihuili Hospital, Ningbo University, Ningbo, Zhejiang 315040, China
[2]Rehabilitation Medicine Center, The Second Affiliated Hospital of Wenzhou Medical University, Wenzhou, Zhejiang 325027, China
[3]Neuroscience Medical Center, Ningbo Medical Center Lihuili Hospital, Ningbo University, Ningbo, Zhejiang 315040, China
[4]Department of Physiology and Pathophysiology, Health Science Center, Ningbo University, Ningbo, Zhejiang 315211, China

Received: 25 December 2024 / Accepted: 4 March 2025
Published online: 13 March 2025

References

1. Hafler DA. Multiple sclerosis. J Clin Invest. 2004;113(6):788.
2. Owens B. Multiple sclerosis. Nature. 2016;540(7631):S1.
3. Marcus R, What. Is Multiple Sclerosis? JAMA. 2022;328(20):2078.
4. Freeman L, Longbrake EE, Coyle PK, Hendin B, Vollmer T. High-Efficacy therapies for Treatment-Naive individuals with Relapsing-Remitting multiple sclerosis. CNS Drugs. 2022;36(12):1285.
5. Bjornevik K, Munz C, Cohen JI, Ascherio A. Epstein-Barr virus as a leading cause of multiple sclerosis: mechanisms and implications. Nat Rev Neurol. 2023;19(3):160.
6. Cortese I, Reich DS, Nath A. Progressive multifocal leukoencephalopathy and the spectrum of JC virus-related disease. Nat Rev Neurol. 2021;17(1):37.
7. Mahad DH, Trapp BD, Lassmann H. Pathological mechanisms in progressive multiple sclerosis. Lancet Neurol. 2015;14(2):183.
8. Kunis G, Baruch K, Rosenzweig N, Kertser A, Miller O, Berkutzki T, et al. IFN-gamma-dependent activation of the brain's choroid plexus for CNS immune surveillance and repair. Brain. 2013;136(Pt 11):3427.
9. Reboldi A, Coisne C, Baumjohann D, Benvenuto F, Bottinelli D, Lira S, et al. C-C chemokine receptor 6-regulated entry of TH-17 cells into the CNS through the choroid plexus is required for the initiation of EAE. Nat Immunol. 2009;10(5):514.

10. Zheng W, Feng Y, Zeng Z, Ye M, Wang M, Liu X, et al. Choroid plexus-selective inactivation of adenosine A(2A) receptors protects against T cell infiltration and experimental autoimmune encephalomyelitis. J Neuroinflammation. 2022;19(1):52.
11. Zheng Y, Hu L, Yang Y, Zheng C, Tu W, Lin H, et al. Blocking the IFN-gamma signal in the choroid plexus confers resistance to experimental autoimmune encephalomyelitis. FASEB J. 2023;37(4):e22833.
12. Robert SM, Reeves BC, Kiziltug E, Duy PQ, Karimy JK, Mansuri MS, et al. The choroid plexus links innate immunity to CSF dysregulation in hydrocephalus. Cell. 2023;186(4):764.
13. Karimy JK, Zhang J, Kurland DB, Theriault BC, Duran D, Stokum JA, et al. Inflammation-dependent cerebrospinal fluid hypersecretion by the choroid plexus epithelium in posthemorrhagic hydrocephalus. Nat Med. 2017;23(8):997.
14. Wang J, Liu R, Hasan MN, Fischer S, Chen Y, Como M, et al. Role of SPAK-NKCC1 signaling cascade in the choroid plexus blood-CSF barrier damage after stroke. J Neuroinflammation. 2022;19(1):91.
15. Bhuiyan MIH, Habib K, Sultan MT, Chen F, Jahan I, Weng Z, et al. SPAK inhibitor ZT-1a attenuates reactive astrogliosis and oligodendrocyte degeneration in a mouse model of vascular dementia. CNS Neurosci Ther. 2024;30(3):e14654.
16. Li Q, Sandoval A, Moth J, Shang J, Liew JY, Dunn T, et al. Reduction of prolonged excitatory neuron swelling after spinal cord injury improves locomotor recovery in mice. Sci Transl Med. 2024;16(766):eadn7095.
17. Yang SS, Huang CL, Chen HE, Tung CS, Shih HP, Liu YP. Effects of SPAK knockout on sensorimotor Gating, novelty exploration, and brain area-dependent expressions of NKCC1 and KCC2 in a mouse model of schizophrenia. Prog Neuropsychopharmacol Biol Psychiatry. 2015;61:30.
18. Yang L, Cai X, Zhou J, Chen S, Chen Y, Chen Z, et al. STE20/SPS1-related proline/alanine-rich kinase is involved in plasticity of GABA signaling function in a mouse model of acquired epilepsy. PLoS ONE. 2013;8(9):e74614.
19. Levit E, Ren Z, Gonzenbach V, Azevedo CJ, Calabresi PA, Cree BA, et al. Choroid plexus volume differentiates MS from its mimics. Mult Scler. 2024;30(8):1072.
20. Jankowska A, Chwojnicki K, Grzywinska M, Trzonkowski P, Szurowska E. Choroid plexus volume Change-A candidate for a new radiological marker of MS progression. Diagnostics (Basel). 2023;13(16).
21. Muller J, Sinnecker T, Wendebourg MJ, Schlager R, Kuhle J, Schadelin S et al. Choroid plexus volume in multiple sclerosis vs neuromyelitis Optica spectrum disorder: A retrospective, Cross-sectional analysis. Neurol Neuroimmunol Neuroinflamm. 2022;9(3).
22. Kahle KT, Khanna AR, Alper SL, Adragna NC, Lauf PK, Sun D, et al. K-Cl cotransporters, cell volume homeostasis, and neurological disease. Trends Mol Med. 2015;21(8):513.
23. Weaver A, Goncalves da Silva A, Nuttall RK, Edwards DR, Shapiro SD, Rivest S, et al. An elevated matrix metalloproteinase (MMP) in an animal model of multiple sclerosis is protective by affecting Th1/Th2 polarization. FASEB J. 2005;19(12):1668.
24. Huang H, Song S, Banerjee S, Jiang T, Zhang J, Kahle KT, et al. The WNK-SPAK/OSR1 kinases and the Cation-Chloride cotransporters as therapeutic targets for neurological diseases. Aging Dis. 2019;10(3):626.
25. Li Y, Hu J, Vita R, Sun B, Tabata H, Altman A. SPAK kinase is a substrate and target of PKCtheta in T-cell receptor-induced AP-1 activation pathway. EMBO J. 2004;23(5):1112.
26. Yan Y, Dalmasso G, Nguyen HT, Obertone TS, Charrier-Hisamuddin L, Sitaraman SV, et al. Nuclear factor-kappaB is a critical mediator of Ste20-like proline-/alanine-rich kinase regulation in intestinal inflammation. Am J Pathol. 2008;173(4):1013.
27. Duval K, Grover H, Han LH, Mou Y, Pegoraro AF, Fredberg J, et al. Modeling physiological events in 2D vs. 3D cell culture. Physiol (Bethesda). 2017;32(4):266.
28. Sellebjerg F, Bornsen L, Ammitzboll C, Nielsen JE, Vinther-Jensen T, Hjermind LE, et al. Defining active progressive multiple sclerosis. Mult Scler. 2017;23(13):1727.
29. Galboiz Y, Shapiro S, Lahat N, Rawashdeh H, Miller A. Matrix metalloproteinases and their tissue inhibitors as markers of disease subtype and response to interferon-beta therapy in relapsing and secondary-progressive multiple sclerosis patients. Ann Neurol. 2001;50(4):443.
30. Saatian B, Deshpande K, Herrera R, Sedighi S, Eisenbarth R, Iyer M, et al. Breast-to-brain metastasis is exacerbated with chemotherapy through blood-cerebrospinal fluid barrier and induces Alzheimer's-like pathology. J Neurosci Res. 2023;101(12):1900.
31. Huang Q, Lan F, Wang X, Yu Y, Ouyang X, Zheng F, et al. IL-1beta-induced activation of p38 promotes metastasis in gastric adenocarcinoma via upregulation of AP-1/c-fos, MMP2 and MMP9. Mol Cancer. 2014;13:18.
32. Tombulturk FK, Soydas T, Sarac EY, Tuncdemir M, Coskunpinar E, Polat E, et al. Regulation of MMP 2 and MMP 9 expressions modulated by AP-1 (c-jun) in wound healing: improving role of Lucilia sericata in diabetic rats. Acta Diabetol. 2019;56(2):177.
33. Bhuiyan MIH, Young CB, Jahan I, Hasan MN, Fischer S, Meor Azlan NF, et al. NF-kappaB Signaling-Mediated activation of WNK-SPAK-NKCC1 cascade in worsened stroke outcomes of Ang II-Hypertensive mice. Stroke. 2022;53(5):1720.
34. Richardson C, Alessi DR. The regulation of salt transport and blood pressure by the WNK-SPAK/OSR1 signalling pathway. J Cell Sci. 2008;121(Pt 20):3293.
35. Gong Y, Wu M, Gao F, Shi M, Gu H, Gao R et al. Inhibition of the p–SPAK/p–NKCC1 signaling pathway protects the blood–brain barrier and reduces neuronal apoptosis in a rat model of surgical brain injury. Mol Med Rep. 2021;24(4).
36. Zhang Z, Wang H, Tao B, Shi X, Chen G, Ma H et al. Attenuation of Blood-Brain barrier disruption in traumatic brain injury via Inhibition of NKCC1 cotransporter: insights into the NF-kappaB/NLRP3 signaling pathway. J Neurotrauma. 2025.
37. Koumangoye R, Penny P, Delpire E. Loss of NKCC1 function increases epithelial tight junction permeability by upregulating claudin-2 expression. Am J Physiol Cell Physiol. 2022;323(4):C1251.
38. Zhang J, Bhuiyan MIH, Zhang T, Karimy JK, Wu Z, Fiesler VM, et al. Modulation of brain cation-Cl(-) cotransport via the SPAK kinase inhibitor ZT-1a. Nat Commun. 2020;11(1):78.
39. Metayer T, Orset C, Ali C, Furon J, Szabla N, Emery E, et al. Bumetanide lowers acute hydrocephalus in a rat model of subarachnoid hemorrhage. Acta Neurochir (Wien). 2022;164(2):499.
40. Donovan MD, Schellekens H, Boylan GB, Cryan JF, Griffin BT. In vitro bidirectional permeability studies identify Pharmacokinetic limitations of NKCC1 inhibitor bumetanide. Eur J Pharmacol. 2016;770:117.
41. Zhang J, Pu H, Zhang H, Wei Z, Jiang X, Xu M, et al. Inhibition of Na(+)-K(+)-2Cl(-) cotransporter attenuates blood-brain-barrier disruption in a mouse model of traumatic brain injury. Neurochem Int. 2017;111:23.
42. Peres DS, Viero FT, Rodrigues P, de Barros Bernardes L, da Silva NAR, Lima IR, et al. Characterization of Depression- and Anxiety-Like behaviours in a mouse model of Relapsing-Remitting multiple sclerosis. J Neuroimmune Pharmacol. 2023;18(3):235.
43. Rangachari M, Kuchroo VK. Using EAE to better understand principles of immune function and autoimmune pathology. J Autoimmun. 2013;45:31.
44. Thomann AS, McQuade CA, Pinjusic K, Kolz A, Schmitz R, Kitamura D, et al. A B cell-driven EAE mouse model reveals the impact of B cell-derived cytokines on CNS autoimmunity. Proc Natl Acad Sci U S A. 2023;120(47):e2300733120.

Publisher's note